processes

MDPI

Article

Stoichiometric Network Analysis of Cyanobacterial Acclimation to Photosynthesis-Associated Stresses Identifies Heterotrophic Niches

Ashley E. Beck [1], Hans C. Bernstein [2] and Ross P. Carlson [3,*]

1 Microbiology and Immunology, Center for Biofilm Engineering, Montana State University, Bozeman, MT 59717, USA; ashley.beck@montana.edu
2 Biological Sciences Division, Pacific Northwest National Laboratory, Richland, WA 99352, USA; hans.bernstein@pnnl.gov
3 Chemical and Biological Engineering, Center for Biofilm Engineering, Montana State University, Bozeman, MT 59717, USA
* Correspondence: rossc@montana.edu; Tel.: +1-406-994-3631

Academic Editor: Michael Henson
Received: 19 April 2017; Accepted: 14 June 2017; Published: 19 June 2017

Abstract: Metabolic acclimation to photosynthesis-associated stresses was examined in the thermophilic cyanobacterium *Thermosynechococcus elongatus* BP-1 using integrated computational and photobioreactor analyses. A genome-enabled metabolic model, complete with measured biomass composition, was analyzed using ecological resource allocation theory to predict and interpret metabolic acclimation to irradiance, O_2, and nutrient stresses. Reduced growth efficiency, shifts in photosystem utilization, changes in photorespiration strategies, and differing byproduct secretion patterns were predicted to occur along culturing stress gradients. These predictions were compared with photobioreactor physiological data and previously published transcriptomic data and found to be highly consistent with observations, providing a systems-based rationale for the culture phenotypes. The analysis also indicated that cyanobacterial stress acclimation strategies created niches for heterotrophic organisms and that heterotrophic activity could enhance cyanobacterial stress tolerance by removing inhibitory metabolic byproducts. This study provides mechanistic insight into stress acclimation strategies in photoautotrophs and establishes a framework for predicting, designing, and engineering both axenic and photoautotrophic-heterotrophic systems as a function of controllable parameters.

Keywords: cross-feeding; cyanobacteria; elementary flux mode analysis; irradiance; resource allocation; RuBisCO; stress acclimation

1. Introduction

Environmental stresses dictate competitive ecological strategies impacting nutrient and energy flows from the scale of individual cells to ecosystems [1,2]. Cyanobacteria are significant drivers of global nutrient and energy flows, accounting for ~10% of global primary productivity [3] and forming essential links in carbon and nitrogen biogeochemical cycles [4]. Cyanobacteria are also used in wastewater treatment and as bioprocess catalysts for bioproduction of specialty chemicals [5,6]. Cyanobacteria are deeply rooted in the tree of life and have adapted competitively to common stressors associated with photosynthesis and are model organisms for examining metabolic acclimation to these stresses.

Photoinhibition is a broad term encompassing different types of photosynthesis-associated stresses including photo-damage by excitation, damage by reactive oxygen species (ROS), and high localized O_2 concentrations [7]. Cyanobacteria can mitigate photo-damage by downregulating

synthesis of photosystems, as well as adjusting relative photon absorption at photosystems I and II (PSI, PSII) to modulate ATP and NADPH regeneration (PSII extracts electrons from water which can be used in conjunction with PSI to regenerate NADPH and ATP, while PSI operating alone recycles electrons to regenerate ATP only; see Figure 1) [8]. High excitation can lead to oxidative damage at the photosystems and/or a highly reduced electron transport chain, which may also lead to cellular oxidative damage via ROS. Acclimation strategies include directing excess electrons toward alternative biochemical routes, such as reduction of O_2 (by either cellular respiration or the water-water cycle (photoreduction of O_2 to water)) or secretion of reduced carbon byproducts. High rates of oxygenic photosynthesis can also lead to locally high O_2 levels [9,10], and environments with high concentrations of O_2 relative to CO_2 can cause additional metabolic stress. Ribulose-1,5-bisphosphate carboxylase oxygenase (RuBisCO) is a dual-functioning enzyme which can react with either CO_2 or O_2. When RuBisCO reacts with O_2, 2-phosphoglycolate is produced, which is either secreted as the inhibitory compound glycolate or catabolized using one of three photorespiration pathways found in cyanobacteria [11]. Cyanobacteria have evolved mechanisms to reduce O_2 consumption at RuBisCO, including species-specific enzymes with varying affinities for CO_2 and O_2, as well as expression of carboxysomes to increase the relative CO_2 concentration in the vicinity of RuBisCO [12,13].

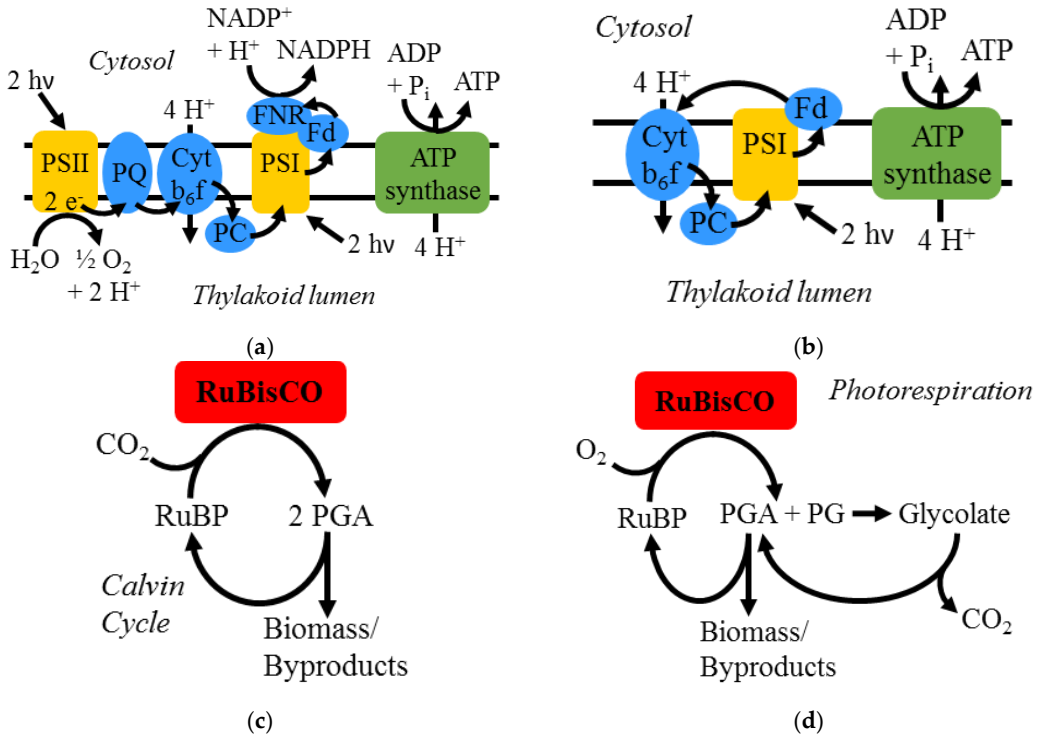

Figure 1. Light and dark reactions of photosynthesis. The role of photosystems I and II (PSI and PSII) in linear (**a**) and cyclic (**b**) photosynthesis and their relation to production of O_2 and regeneration of NADPH and ATP. Linear photosynthesis produces O_2 and regenerates both ATP and NADPH, whereas cyclic photosynthesis does not produce O_2 and regenerates ATP only. In the dark reactions, the bifunctional RuBisCO enzyme can incorporate inorganic carbon into biomass via the Calvin cycle (**c**) or can react with O_2 (**d**), resulting in a toxic byproduct and reducing incorporation of carbon into biomass. Abbreviations: hν, photons (photosynthetically active radiation); PQ, plastoquinone/plastoquinol; Cyt b_6f, cytochrome b_6f; PC, plastocyanin; FNR, ferredoxin-$NADP^+$ reductase; Fd, ferredoxin; RuBP, ribulose-1,5-bisphosphate; PGA, 3-phosphoglycerate; PG, 2-phosphoglycolate.

Stoichiometric modeling of metabolism enables prediction and interpretation of system-wide properties of complex metabolic networks, including community-level networks [14–20]. These systems biology approaches, such as flux balance analysis (FBA) and elementary flux mode

analysis (EFMA), use genomic and physiological data to inform the construction of computational representations of metabolism. The application of a steady state assumption simplifies the mass-balanced metabolic reactions into a series of solvable linear equations, reducing the need for difficult-to-measure, condition-dependent enzyme kinetic parameters [16]. Whereas FBA uses objective functions such as biomass production to predict an optimal flux distribution under a specific set of conditions, EFMA calculates the complete set of minimal pathways (elementary flux modes, EFMs) through a metabolic network using steady state, reaction reversibility, and indecomposability constraints. Non-negative linear combinations of EFMs define the entire phenotypic solution space of a steady state metabolic network using a single simulation and can be used to examine all possible physiologies in an unbiased manner [19,21]. Similarities and differences in the output of EFMA versus other stoichiometric modeling techniques can be found in the review by Trinh et al. [19]. The enumerated EFMs can be evaluated by resource allocation theory, which quantitatively assesses the computational phenotypic space according to tradeoffs in consumption of different resources for the production of bioproducts [22–26]. Previous stoichiometric modeling studies of cyanobacterial metabolism have examined the occurrence of photorespiration as well as irradiance and carbon limitations [27–30].

The presented study analyzes metabolic acclimation to photosynthesis-associated stresses in the thermophilic, non-diazotrophic unicellular cyanobacterium *Thermosynechococcus elongatus* BP-1 (hereafter BP-1) and the formation of heterotrophic niches. BP-1 was isolated from the alkaline (pH 8.6) Beppu hot springs in Japan where temperatures range from 50–65 °C [31,32]. BP-1 is a major primary producer in its native hot springs where it often grows in bacterial mat communities with heterotrophs and is subject to high irradiance, high O_2, and low nutrient availability stresses. The objectives of this study were to (i) identify ecologically relevant acclimation strategies to high irradiance, O_2/CO_2 competition at RuBisCO, and nutrient limitation at varying degrees using a computational BP-1 stoichiometric model and EFMA combined with resource allocation theory, (ii) analyze BP-1 acclimation to high irradiance through controlled photobioreactors, (iii) compare general computational predictions to specific photobioreactor observations to interpret BP-1 acclimation strategies, and (iv) examine the impact of stress acclimation strategies on the ability of BP-1 to interact with heterotrophic partners. The presented study contributes to the understanding of cyanobacterial metabolism by examining specific photorespiration pathways, relative photon absorption of the photosystems, and byproduct secretion profiles under simultaneous stress conditions of high irradiance and O_2/CO_2 competition at RuBisCO, as well as by predicting cross-feeding photoautotrophic-heterotrophic interactions. The computational resource allocation-based modeling integrated with photobioreactor observations provides a rational basis for interpreting natural cyanobacterial behavior and a framework for controlling cyanobacteria for bioprocess applications.

2. Materials and Methods

2.1. Photobioreactor Culturing

T. elongatus BP-1 cultures were grown using modified BG-11 (mBG-11) medium [33,34], containing 17.6 mM $NaNO_3$, 0.304 mM $MgSO_4 \cdot 7H_2O$, 0.175 mM KH_2PO_4, 0.245 mM $CaCl_2 \cdot 2H_2O$, 0.0028 mM Na_2EDTA, and 0.0144 mM $FeCl_3$. A trace metal supplement was added (1 mL/L), comprised of 46.254 mM H_3BO_3, 9.146 mM $MnCl_2 \cdot 4H_2O$, 0.772 mM $ZnSO_4 \cdot 7H_2O$, 1.611 mM $Na_2MoO_4 \cdot 2H_2O$, 0.316 mM $CuSO_4 \cdot 5H_2O$, and 0.170 mM $Co(NO_3)_2 \cdot 6H_2O$. Inoculum cultures of BP-1 were initiated from frozen stocks into 150-mL sealed serum bottles filled with 50 mL mBG-11 amended with 15 mM sodium bicarbonate and adjusted to pH 7.5 under N_2 headspace containing 10% CO_2.

Photobioreactors were operated as turbidostats as described in Bernstein et al. [33], similar to Bernstein et al. and Melnicki et al. [35,36]. Reactors were inoculated with exponentially growing inoculum culture to OD_{730nm} = 0.01. All cultures were grown under continuous light of varying irradiances at 52 °C, pH 7.5, and were continuously sparged at 4 L min^{-1} with a 98% N_2 and 2%

CO_2 gas mixture. Incident and transmitted scalar irradiances were measured and used to adjust the turbidostat growth rate. The specific optical cross section (σ, m^2 (g CDW)$^{-1}$, CDW, cell dry weight) was determined according to a previously described method using a light diffuser and spectrophotometer [37]. The specific photon absorption rate was calculated by multiplying the specific optical cross section by the incident irradiance.

2.2. Biomass Composition Determination

Macromolecular composition was analyzed from turbidostat biomass samples (pelleted and frozen at Pacific Northwest National Laboratory and then shipped to Montana State University for subsequent analysis) according to the following procedures. DNA was quantified from alkali-lysed solutions with Hoechst 33258 fluorescent dye [38]. Glycogen was quantified by co-precipitation with sodium sulfate and detection with anthrone [39]. Lipids were quantified gravimetrically via chloroform-methanol extraction [40]. Total protein and amino acid distribution were quantified with HPLC fluorescence detection using *o*-phthalaldehyde (OPA) and 9-fluorenylmethylchloroformate (FMOC) derivatizations of acid-hydrolyzed protein [41]. Cysteine, methionine, and tryptophan were degraded, and asparagine and glutamine were converted to aspartate and glutamate, respectively, during hydrolysis [42]; therefore, abundances were predicted from protein-coding gene codon usage. RNA was quantified by lysis with potassium hydroxide, extraction into cold perchloric acid, and measurement of UV absorbance at 260 nm [43]. Appendix A contains detailed protocols for each method.

2.3. Model Construction

The metabolic network model for BP-1 was constructed in CellNetAnalyzer [44,45] from the annotated genome [46] with the aid of MetaCyc, KEGG, BRENDA, and NCBI databases [47–49]. Reversible exchange reactions were defined for protons and water. Irreversible exchange reactions defined bicarbonate, magnesium, nitrate, phosphate, photons, and sulfate as possible substrates and O_2, acetate, alanine, ethanol, formate, glycolate, lactate, pyruvate, and sucrose as possible byproducts. Biomass was also defined as a product.

Macromolecular synthesis reactions were defined for nucleic acids, glycogen (most common form of cyanobacterial carbohydrate storage [50]), lipid, and protein. Synthesis reactions utilized two phosphate bonds per nucleic acid monomer, one phosphate bond per glycogen monomer, and four phosphate bonds per protein monomer [51]. Nucleotide distributions were set based on percent GC content of the genome for DNA and nucleotide sequence of the rRNA genes for RNA. Fatty acid distribution was assigned based on literature values of fatty acid chain and lipid types measured for BP-1 [52–54]. The amino acid distribution was set using the experimentally measured values in the current study. Macromolecular composition (DNA, glycogen, lipid (including chlorophyll), protein, and RNA) was determined experimentally in the current study (see Section 2.2) and used to set the molar coefficients in the biomass synthesis reaction, normalized to 1 kg dry biomass (File S1 in the Supplementary Materials). Chlorophyll was also included in biomass synthesis using the mass fraction measured for *Synechococcus* sp. PCC 7002 [29], and the lipid mass fraction was adjusted to reflect the proportion of chlorophyll. The biomass composition was converted into an electron requirement using degree of reduction (moles of electrons per mole of carbon) calculations [55] with the assumption that each biosynthetic electron requires two photons (one absorbed at each PSII and PSI). Degree of reduction was calculated with respect to nitrate as a nitrogen source. To estimate photons necessary for ATP regeneration, the phosphate bond requirement for polymerization of monomers into macromolecules was converted into a photon requirement via a stoichiometry of four photons per phosphate bond (one photon absorbed at PSI per proton pumped, with four protons translocated per ATP molecule synthesized). Photon and proton stoichiometries remain active areas of research, and this estimate is recognized as an upper bound considering linear photosynthesis without a Q-cycle [56,57].

All reactions were balanced for elements, charge, and electrons. Thermodynamic considerations were built into the model via reaction reversibilities, based on data from BRENDA [49]; in the

event that data for bacterial species were not available from BRENDA, thermodynamic calculations were performed with eQuilibrator (http://equilibrator.weizmann.ac.il/) to determine physiological reversibility, using a product concentration three orders of magnitude greater than the reactant concentration [58,59]. Nitrogen requirements were determined for each reaction by summing the number of nitrogen atoms specified by the enzyme amino acid sequences. Iron requirements were determined for central carbon metabolism and photosynthesis reactions based on metal requirements of similar cyanobacterial species in BRENDA [49]. For instances of missing or conflicting information in the database, literature values compiled for oxygenic photoautotrophs were used [60]. A one-to-one (minimal resource investment) correspondence of enzyme to reaction was used to calculate the total cost per EFM, as it has previously been shown to provide a good approximation of flux distributions in *Escherichia coli* [23,24]. EFMs were enumerated using EFMtool [61]. Resource allocation analysis (cost assessment) of the resulting EFMs was performed with MATLAB and Python. The metabolic model with supporting details and CellNetAnalyzer metabolite and reaction input, SBML model version, and documented analysis routines can be found in the Supplementary Materials (Files S1–S4).

3. Results

3.1. Computational BP-1 Metabolic Model and Photobioreactor Biomass Composition Measurement

The BP-1 computational metabolic model was constructed from the annotated genome [46]. Genetic potential was mapped to enzymes and metabolic reactions which encompassed photosynthesis, central metabolism, and biosynthetic reactions leading to biomass production according to a defined macromolecular composition reaction. Transport reactions were defined for nutrient uptake and product secretion. Subsequent EFMA resulted in a description of the phenotypic space spanning the range of possible nutrient uptake and product secretion rates, which could then be analyzed for ecologically relevant stress acclimation strategies. The model accounted for 334 metabolism-associated genes which were mapped to 279 metabolites and 284 reactions (File S1 in the Supplementary Materials). Photons were assumed to be within the spectrum of photosynthetically active radiation (PAR; 400–700 nm). A stoichiometrically balanced schematic demonstrating operation of the photosynthetic electron transport chain (linear and cyclic photosynthesis) and carbon flow in the model is shown in Figure 1. Nutrient substrates for the model were selected in alignment with the photobioreactor culturing medium. Bicarbonate was modeled as the sole carbon source based on culturing pH while interconversion with CO_2 was modeled via the carboxysomal carbonic anhydrase enzyme, and nitrate was modeled as the sole nitrogen source. Two of the three photorespiration pathways possible in cyanobacteria [11] were identified in BP-1, namely, the C2 cycle and the glycerate pathway. A variety of organic byproducts (Table 1) were considered based on previous genomic analysis of BP-1 [62] and culturing studies of related unicellular cyanobacteria [63,64]. Secretion of several different amino acids has been observed in BP-1 and related species [33,63,64]; alanine was included as a representative amino acid byproduct in the current model, closely linked to central metabolism.

Biomass composition impacts growth and byproducts [65], making appropriate composition parameters important for computational growth predictions. BP-1 macromolecular biomass composition was determined analytically from continuous culture samples and was used to parameterize the model growth reactions. The major measured macromolecule classes (DNA, glycogen, lipid (including chlorophyll), protein, and RNA) summed to 98.1% of cell dry weight (Table 2); the remaining 1.9% was assumed to be ash. Protein and lipid/chlorophyll comprised the largest mass fractions of biomass, accounting for 62.0% and 17.4%, respectively. Since protein comprises the largest fraction of biomass, amino acid monomer distribution was also determined analytically (Table A1 in Appendix C) and used to parameterize the model reaction for protein synthesis. A strong correlation was observed between the measured amino acid distribution and the distribution predicted from protein-coding gene sequences (Figure A1 in Appendix B).

Table 1. *T. elongatus* BP-1 metabolic model inputs and outputs, including potential reduced carbon byproducts, with corresponding degree of reduction.

	Compound	Formula	Charge	Degree of Reduction
Inputs	Carbon dioxide	CO_2	0	0
	Water	H_2O	0	0
	Photons	NA	NA	NA
	Nitrate	NO_3	−1	−8/−5/0
Outputs	Molecular oxygen	O_2	0	−4
	Biomass	$CH_{1.6}N_{0.2}O_{0.3}P_{0.01}S_{0.005}$	−0.7	4.3/5.0/6.1 [a]
	Acetate	$C_2H_3O_2$	−1	4
	Alanine	$C_3H_7NO_2$	0	4/5/6.7 [a]
	Ethanol	C_2H_6O	0	6
	Formate	CHO_2	−1	2
	Glycolate	$C_2H_3O_3$	−1	3
	Lactate	$C_3H_5O_3$	−1	4
	Pyruvate	$C_3H_3O_3$	−1	3.3
	Sucrose	$C_{12}H_{22}O_{11}$	0	4

[a] Degree of reduction calculated with respect to ammonia/molecular nitrogen/nitrate. NA, not applicable.

Table 2. Experimentally determined *T. elongatus* BP-1 biomass composition from turbidostat biomass samples grown under an irradiance of 2000 µmol photons m^{-2} s^{-1}.

Macromolecule	Mass Percent	Extraction Method/Analytical Method
DNA	0.4	Alkaline lysis/Hoechst 33258 fluorescence
Glycogen	2.0	Sodium sulfate co-precipitation/Anthrone detection
Lipid (including chlorophyll)	17.4	Chloroform-methanol/Gravimetric
Protein	62.0	Hydrochloric acid hydrolysis/OPA, FMOC derivatization
RNA	16.3	Alkaline lysis, perchloric acid/UV absorbance
Total	98.1	

3.2. Computational Analysis of Stress Acclimation

The computational BP-1 metabolic model was decomposed into 4,636,498 unique EFMs using EFMtool [61], with ~99.5% producing biomass. Each EFM, as well as any non-negative linear combination of multiple EFMs, represented a mathematically feasible phenotype and possible stress acclimation strategy. Competitive stress acclimation strategies were identified using ecological resource allocation theory. Resource allocation theory analyzes the amount of catabolic or anabolic resource required to synthesize a cellular product, often biomass. Minimizing the requirement of a limiting resource represents a competitive, cost-effective phenotype and is hypothesized to be a probable cellular strategy selected by evolution. When two or more resources are considered simultaneously, a multi-dimensional tradeoff surface is created that quantifies the utilization relationship between the limiting resources [22–25]. Biomass-producing EFMs were ranked quantitatively based on efficiency of resource use for biomass production under simulated environmental stresses including high irradiance, O_2/CO_2 competition at RuBisCO, and limited availability of dissolved inorganic carbon (DIC) as well as nitrogen or iron. The tradeoff between optimal use of two resources was quantified by simultaneously minimizing the cost of biomass production under two different stress factors. Similar methods have been applied to extend FBA to account for biosynthetic costs [26], but enumeration of complete EFMs combined with resource allocation theory allows exploration of the entire phenotypic space.

3.2.1. Irradiance and Photosynthetic Electron Flow

Photosynthetic electron flow was examined as a function of irradiance-induced stress to interpret relationships between photon absorption and photocatalytic water oxidation. Net O_2 production per carbon mole (Cmol) biomass produced was plotted as a function of photons absorbed per Cmol biomass produced, a metric of irradiance-induced stress (Figure 2). Each net O_2 molecule is the byproduct of four photosynthetically derived electrons extracted from water and requires eight total photons absorbed [66]; this relationship is reflected in the slope of the upper boundary of the phenotypic cone. Photons absorbed at PSI during cyclic photosynthesis are decoupled from O_2 production. Growth phenotypes were analyzed for the ability to direct electrons toward either biomass or reduced byproducts. The EFMs along the lowest boundary of the phenotypic cone in Figure 2 represented growth where all electrons were directed to biomass and no reduced byproducts were secreted, extending up to ~80 mol photons absorbed per Cmol biomass produced. Net O_2 production (~1.53 mol O_2 per Cmol biomass) at the lowest boundary corresponds to the biomass degree of reduction, ~6.1 mol electrons available to reduce O_2 per Cmol biomass (Table 1). EFMs with higher net O_2 production directed electrons to reduced carbon byproducts, such as formate or acetate.

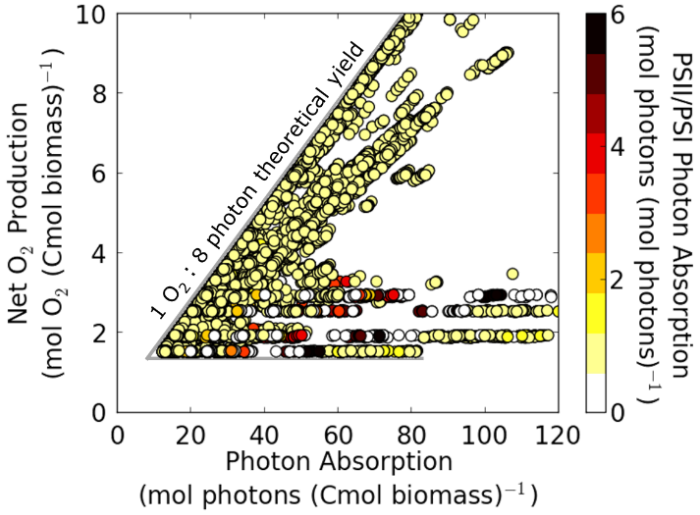

Figure 2. Computational analysis of irradiance and photosynthetic electron flow in cyanobacterium *T. elongatus* BP-1. Net O_2 production (net mol O_2 evolved (Cmol biomass produced)$^{-1}$) is plotted as a function of photon absorption (mol photons absorbed (Cmol biomass produced)$^{-1}$) for biomass-producing EFMs. Each point represents a unique EFM. The slope of the upper boundary of the phenotypic cone indicates maximum net moles of O_2 produced per mole of photons absorbed (eight photons required per molecule O_2 evolved; theoretical minimum quantum requirement). No byproducts were secreted on the lower boundary of the phenotypic cone minimizing net O_2 production per biomass produced; net O_2 production along this boundary was a direct result of electrons incorporated into biomass; secreted reduced carbon byproducts were predicted throughout the remaining phenotypic space. Color scale represents the photon absorption at PSII relative to PSI for each EFM (mol photons absorbed at PSII (mol photons absorbed at PSI)$^{-1}$). Relative contribution of PSII was predicted to increase as photon absorption increased. Less than 1% of the EFMs had a PSII/PSI ratio greater than 6 (with maximal value of 20) and were excluded from the plot to represent a more feasible phenotypic space [67–69]. Modeled biomass production did not include maintenance energy requirements. Points in the plot area shown are representative of 4,371,798 EFMs.

Biomass-producing EFMs were assessed for photon absorption at PSII relative to PSI to quantify the contribution of the two photosystems to photosynthetic electron flow (Figure 2, shaded color bar). A value less than one indicated elevated cyclic photosynthesis, a value greater than one indicated elevated operation of PSII independent of linear photosynthesis (i.e., reduction of O_2 through either

cellular respiration or the water-water cycle), and a value equal to one indicated linear photosynthesis or, alternatively, equivalent cyclic photosynthesis and O_2 reduction. Figure 1 provides greater detail on cyclic and linear photosynthesis. An increase in photon absorption at PSII at a fixed net O_2 production indicated greater gross production of O_2, which was consumed by cellular respiration and/or the water-water cycle. In general, photon absorption at PSII relative to PSI was predicted to increase as irradiance-induced stress increased (Figure 2), indicating a greater contribution of PSII to photon absorption at high irradiance.

3.2.2. Irradiance, High O_2, and Nutrient Limitation

Computational BP-1 growth phenotypes were interrogated for stress acclimation strategies under a range of relative O_2 to DIC concentrations, represented by O_2/CO_2 competition at RuBisCO (Figure 3a). The tradeoff curve simultaneously minimizes the cost of biomass production under O_2/CO_2 competition (moles O_2 per mole CO_2 consumed at RuBisCO) and irradiance-induced stress; EFMs on the tradeoff curve (or non-negative linear combinations thereof) represent optimal predicted growth phenotypes under the combined stresses. Photorespiration, as opposed to secretion of glycolate, was predicted as an essential process on the tradeoff curve except at zero O_2/CO_2 competition, and utilization of photorespiration reactions increased with increasing stress. Utilization of the C2 photorespiration cycle was predicted to increase along the tradeoff curve, whereas use of the glycerate pathway remained minimal. Photon absorption at PSII relative to PSI was also predicted to increase along the tradeoff curve. Neither cellular respiration nor the water-water cycle was active along the tradeoff curve, indicating that all photosynthetically derived electrons were directed to either biomass or reduced carbon byproducts. The tradeoff curve was divided into four phenotypic zones based on the suite of byproducts predicted. Zone 1 phenotypes did not secrete reduced byproducts, but as O_2/CO_2 competition at RuBisCO increased, more energy from photons was required to mediate the stress as indicated by higher photon absorption per biomass. At high O_2/CO_2 competition (~0.8 mol O_2 (mol CO_2)$^{-1}$), byproduct secretion represented the most resource-efficient acclimation strategy under the combined stresses. Byproduct synthesis effectively consumed photosynthetically derived electrons at the expense of fixed DIC and, conditionally, reduced nitrogen, as seen in the transition in byproducts produced along the tradeoff curve. Formate was predicted to be the most resource-efficient byproduct (zone 2 phenotypes), followed by combinations of formate and amino acids, represented in the model as alanine (zone 3 phenotypes), and acetate and amino acids (zone 4 phenotypes). Secretion of glycolate was not the most competitive use of metabolic potential under the considered stresses. Net O_2 production of the tradeoff curve EFMs quantified the fraction of electrons directed to biomass and reduced byproducts as a function of stress acclimation (Figure 3b). A nonlinear increase in net O_2 production per Cmol biomass was predicted; the increase in net O_2 production correlated with the secretion of reduced byproducts (formate, acetate, and/or alanine).

In addition to DIC, nitrogen and iron are essential anabolic resources and place constraints on cellular functions such as growth or ATP regeneration [70]. Acclimation to nitrogen- or iron-limited growth, assessed by investment into enzymes, was analyzed in conjunction with O_2/CO_2 competition (Figure A2a,b in Appendix B). Increasing O_2/CO_2 competition at RuBisCO necessitated an increase in nitrogen and iron investments into metabolic enzymes due to the requirement to process 2-phosphoglycolate. Tradeoff curve analysis of simultaneous acclimation to O_2/CO_2 competition and nutrient limitation showed trends similar to those predicted under irradiance-induced stress in Figure 3a, and amino acid secretion was again predicted at the highest resource limitation stress. However, under nitrogen limitation, reduced byproduct secretion was required for the most competitive phenotypes over the entire range of resource-limited growth. BP-1 metabolism was predicted to be less robust to nitrogen-limited stress than irradiance-induced stress as indicated by relatively fewer suboptimal EFMs near the tradeoff curve (Figure A2a in Appendix B). Additional details on nitrogen and iron limitation are found in Appendix D. While the majority of EFMs produced

biomass, energy-producing EFMs (not producing biomass) also showed similar optimal byproducts under irradiance-induced stress and O_2/CO_2 competition (data not shown).

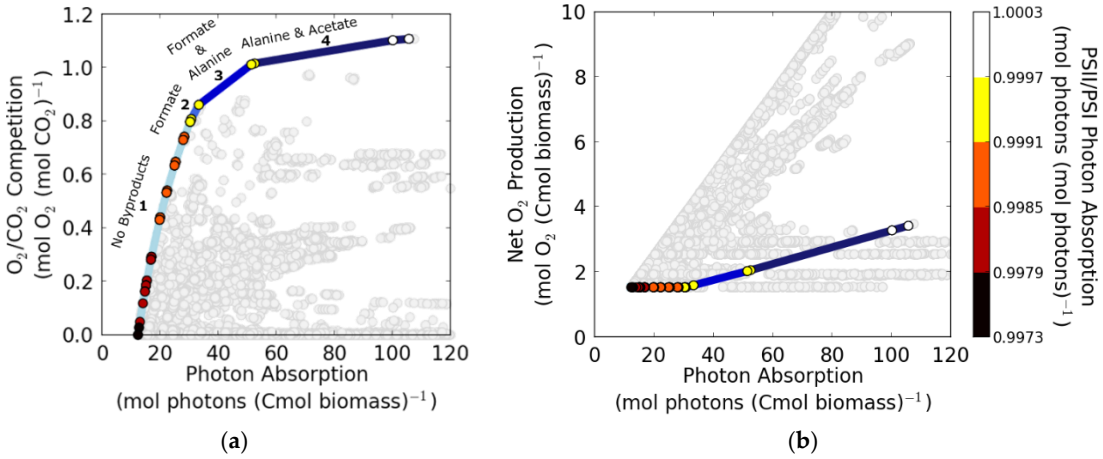

Figure 3. Computational analysis of irradiance-induced stress and O_2/CO_2 competition at RuBisCO in cyanobacterium *T. elongatus* BP-1. (**a**) O_2/CO_2 competition at RubisCO (mol O_2 (mol CO_2)$^{-1}$ consumed) as a function of photon absorption (mol photons absorbed (Cmol biomass produced)$^{-1}$) for biomass-producing EFMs are plotted. Each point represents a unique EFM. The tradeoff curve defining competitive strategies between O_2/CO_2 competition and irradiance-induced stress was divided into four distinct phenotypic regions based on byproduct secretion behavior, labeled accordingly (intensity of shading increases with increasing stress). The maximum amount of O_2 per CO_2 consumption at RuBisCO that can be sustained is two to one. Consumption of two O_2 molecules followed by photorespiration recycles 2-phosphoglycolate to regenerate the ribulose-1,5-bisphosphate precursor, but loses the single molecule of CO_2 that was consumed and thus cannot support biomass production. Points in the plot area shown are representative of 4,457,199 EFMs. (**b**) Net O_2 production (net mol O_2 evolved (Cmol biomass produced)$^{-1}$) as a function of photon absorption (mol photons absorbed (Cmol biomass produced)$^{-1}$) for biomass-producing EFMs are plotted. Colored points indicate net O_2 production of EFMs on the tradeoff curve in (**a**). Color scale represents the photon absorption at PSII relative to PSI (mol photons absorbed at PSII (mol photons absorbed at PSI)$^{-1}$). Modeled biomass production did not include maintenance energy requirements. Points in the plot area shown are representative of 4,355,094 EFMs.

3.3. Comparison of Computational Predictions with Photobioreactor Physiological Data

The optimal predicted growth phenotypes identified along the tradeoff curve (Figure 3a) were compared with data from turbidostat culturing experiments. Irradiance levels altered both specific growth rate and biomass yield during cultivation. Specific growth rates ranged from 0.06–0.29 h^{-1} at irradiances varying from 200–2000 µmol photons m^{-2} s^{-1} (Figure 4a). Specific growth rates increased linearly as a function of incident irradiance below 500 µmol photons m^{-2} s^{-1}. Above 500 µmol photons m^{-2} s^{-1}, irradiance became saturating, possibly inhibitory, and specific growth rate approached a maximum at 1800–2000 µmol photons m^{-2} s^{-1}. Conversely, biomass yield per photon absorbed had a maximum at low irradiance (200–300 µmol photons m^{-2} s^{-1}) and decreased nonlinearly as a function of incident irradiance (Figure 4b). Irradiance-induced stress at 2000 µmol photons m^{-2} s^{-1} reduced the biomass production efficiency by more than 50% compared to low irradiance conditions. The decrease in biomass per photon yield is consistent with predicted acclimation strategies, as is the nonlinear relationship between stress and biomass growth efficiency (Figure 3).

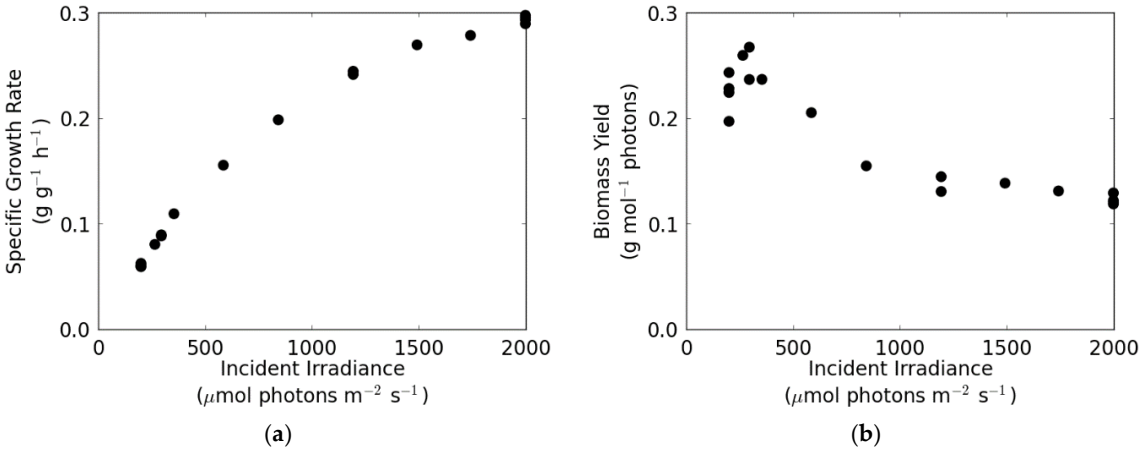

Figure 4. Photobioreactor impact of irradiance on specific growth rate and biomass production efficiency in *T. elongatus* BP-1 continuous culture. (**a**) Photobioreactor measurement of BP-1 specific growth rate (g CDW (g CDW)$^{-1}$ h^{-1}) as a function of incident irradiance (µmol photons m^{-2} s^{-1}). CDW, cell dry weight. (**b**) Photobioreactor measurement of BP-1 biomass yield (g CDW (mol photons absorbed)$^{-1}$) as a function of incident irradiance (µmol photons m^{-2} s^{-1}).

BP-1 maintenance energy requirements were estimated by analyzing specific photon absorption rate as a function of specific growth rate (Figure 5). The non-growth associated maintenance energy requirement (0.16 mol photons (g CDW)$^{-1}$ h^{-1}) was estimated by extrapolating the specific photon absorption rate data to a zero growth rate. Photon requirements for growth can be partitioned into the cellular energy required to (1) reduce nutrients such as DIC and nitrate into biomass monomers and (2) polymerize monomers into macromolecules. The photon requirement to reduce nutrient substrates, including bicarbonate and nitrate, to biomass monomers was calculated using the experimentally measured biomass composition. Macromolecular synthesis reactions in the model incorporated the energy cost of phosphate bonds required to polymerize monomers.

Photon requirement per Cmol biomass increased nonlinearly at higher growth rates (Figure 5), which corresponded to higher incident irradiance and represented successively increasing irradiance-induced stress and reduced biomass production efficiency. The difference between the photon requirement for biomass and the experimentally measured photon requirement is hypothesized to be the photon requirement for growth-associated maintenance energy, including tasks such as general protein repair, enzyme turnover, and maintenance of gradients, or other drains such as non-photochemical quenching of absorbed photons [8,71–73]. Additionally, the repair and recycling of PSII due to increased photoinactivation at high irradiance requires a large investment of nitrogen and poses a significant limitation on growth [74,75]. The implications of nitrogen source degree of reduction were also factored into maintenance energy calculations. A comparison of the effects of different nitrogen sources on the photon requirement is shown in Figure A3 in Appendix B. Molecular nitrogen and ammonia required fewer photons per biomass since they are more reduced than nitrate. Nitrate may be a preferred nitrogen source for photoautotrophs under high irradiance conditions, likely because it represents a possible sink for electrons which can buffer over-reduced photosynthetic machinery.

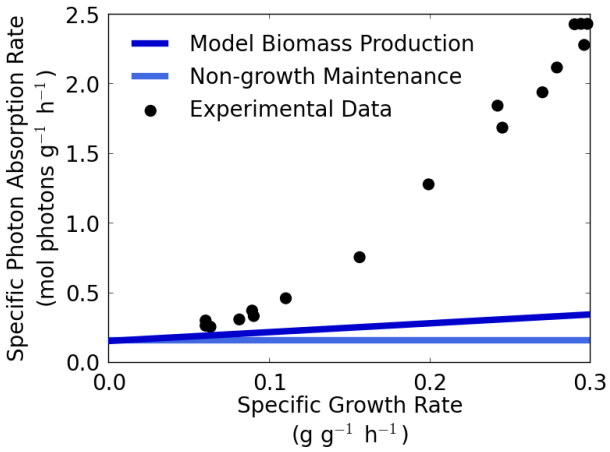

Figure 5. Growth rate-dependent photon absorption rate and maintenance energy in cyanobacterium *T. elongatus* BP-1. Specific photon absorption rate (mol photons absorbed (g CDW)$^{-1}$ h^{-1}) is plotted as a function of specific growth rate (g CDW (g CDW)$^{-1}$ h^{-1}) for experimental BP-1 turbidostat cultures (black circles). Specific photon absorption rate is dependent on specific growth rate (μ) according to the equation $0.16e^{9.47\mu}$ determined from an exponential regression of the photobioreactor data. The non-growth associated maintenance energy requirement was extrapolated from a specific growth rate of zero (light blue line). Measured photon absorption rates are contrasted with calculated requirements for biomass synthesis, including polymerization (dark blue line). CDW, cell dry weight.

3.4. Comparison of Computational Predictions with Photobioreactor Transcriptomic Data

The optimal predicted growth phenotypes identified along the tradeoff curve (Figure 3a) were compared with previously published BP-1 transcriptomic data [33]. The transcriptomic data were analyzed for differentially expressed genes (two-fold or greater difference) between high and low irradiance conditions (2000 versus 200 μmol photons m^{-2} s^{-1}). A change in expression of two-fold or greater was observed for 1147 genes. Differentially expressed genes were examined according to metabolic pathways and compared with the pathways utilized in the predicted optimal stress acclimation phenotypes. Consistencies and inconsistencies between predicted and observed metabolic functionalities were grouped into six categories (Table 3) and are discussed in detail below.

Table 3. Comparison between computational predictions of stress acclimations and previously published photobioreactor gene expression data under high versus low irradiance conditions [33]. Metabolic functionalities were predicted from competitive pathways along the optimal tradeoff curve for irradiance-induced stress and O_2/CO_2 competition (Figure 3a), and observations were made from gene expression data comparing change in transcripts from high to low irradiance (2000 versus 200 μmol photons m^{-2} s^{-1}) [33].

	Prediction	Observation
1. Photosystem contribution	• Increased PSII photon absorption relative to PSI	• Upregulation of PSII-associated genes • No change in PSI-associated genes
2. Photorespiration pathways	• Use of photorespiration • Increase in photorespiration with higher O_2/CO_2 competition	• Transcription of photorespiration genes • Upregulation of C2 cycle genes
	• Primarily C2 cycle, minimal glycerate pathway usage	• No change in glycerate pathway genes
3. Byproduct secretion	• Production of reduced byproducts• Formate and acetate production	• Upregulation of formate, acetate, and sucrose synthesis genes
	• Amino acid (alanine) secretion at highest stress	• Upregulation of amino acid synthesis pathway and transporter genes

Table 3. *Cont.*

	Prediction	Observation
4. Glycolysis	• Increased use of lower portion of glycolysis	• Upregulation of genes in lower portion of glycolysis
5. TCA cycle	• No change in TCA cycle use	• Upregulation of TCA cycle genes leading to synthesis of α-ketoglutarate
6. Nitrate and sulfate assimilation	• Increased nitrate uptake in pathways that secrete amino acid byproducts • No change in sulfate uptake	• Upregulation of nitrate uptake and assimilation genes • Upregulation of sulfate uptake and assimilation genes

3.4.1. Photosynthesis, Photorespiration, and Byproducts

The predicted increase in photon absorption at PSII relative to PSI (Figure 3a) was reflected in the transcriptomic data [33] showing upregulation of genes coding for several PSII subunit and repair genes but no upregulation of PSI-associated genes (Table A2 in Appendix C). The increase in transcript level could be due to increased photon absorption, or it could reflect an increased turnover of PSII, which has been reported during culturing at high irradiance [74,75]. A relative increase in photon absorption at PSII would suggest an increased relative contribution of PSII to photosynthetic electron flow under irradiance-induced stress. Photorespiration was a predicted strategy under high irradiance and O_2/CO_2 competition, corresponding to upregulation of photorespiration pathway genes observed in the transcriptomic data [33]. Predicted pathways indicated preferential utilization of the C2 photorespiration cycle as opposed to the glycerate pathway, and transcriptomic data [33] indicated upregulation of C2 cycle genes with no change in expression of glycerate pathway genes (Figure 6). Byproduct secretion was predicted as a competitive strategy at high irradiance and O_2/CO_2 competition. Irradiance, nitrogen investment, and iron investment analyses in conjunction with O_2/CO_2 competition all predicted amino acid secretion as a resource-efficient strategy at the highest combined stress conditions (Figures 3a and A2). These predictions corresponded with observations of upregulated genes for synthesis pathways of organic compounds such as acetate and formate (Figure 6), as well as for more than 50 amino acid synthesis pathway and transporter genes (Table A3 in Appendix C). Altogether, these parallels with the transcriptomic data [33] suggest increased electron flow into the system, increased photorespiration, and reprocessing of salvaged carbon into other byproducts with greater degree of reduction (Table 1) at higher irradiance.

3.4.2. Central Metabolism and Nutrient Assimilation

Several glycolysis genes were observed to be upregulated under high irradiance conditions [33], primarily genes involved in the lower portion of glycolysis after glyceraldehyde-3-phosphate (glyceraldehyde-3-phosphate dehydrogenase, phosphoglycerate kinase, phosphoglycerate mutase, enolase, and pyruvate kinase) (Table A2 in Appendix C). Tradeoff curve analysis of the EFMs under high irradiance and O_2/CO_2 competition predicted that utilization of the reactions catalyzed by these enzymes increased with increasing stress except for glyceraldehyde-3-phosphate dehydrogenase. Both glyceraldehyde-3-phosphate and 3-phosphoglycerate intersect the Calvin cycle and glycolysis; thus, increased use of the lower portion of glycolysis suggested funneling of glyceraldehyde-3-phosphate from the Calvin cycle into glycolysis to produce pyruvate, which may be used to synthesize byproducts such as formate, acetate, and amino acids. Several TCA cycle genes were also observed to be upregulated under high irradiance conditions, predominantly genes catalyzing reactions up to the synthesis of α-ketoglutarate, from which several amino acids are synthesized (Table A2 in Appendix C). Tradeoff curve analysis of the EFMs under high irradiance and O_2/CO_2 competition predicted no change in utilization of any TCA cycle reactions. The BP-1 model utilized alanine as a representative amino acid which could be secreted as a byproduct; alanine is synthesized via pyruvate. However, if the computational model was modified to allow secretion of amino acids that are synthesized via

TCA cycle intermediates, such as glutamate, it would lead to predictions of increases in some TCA cycle fluxes.

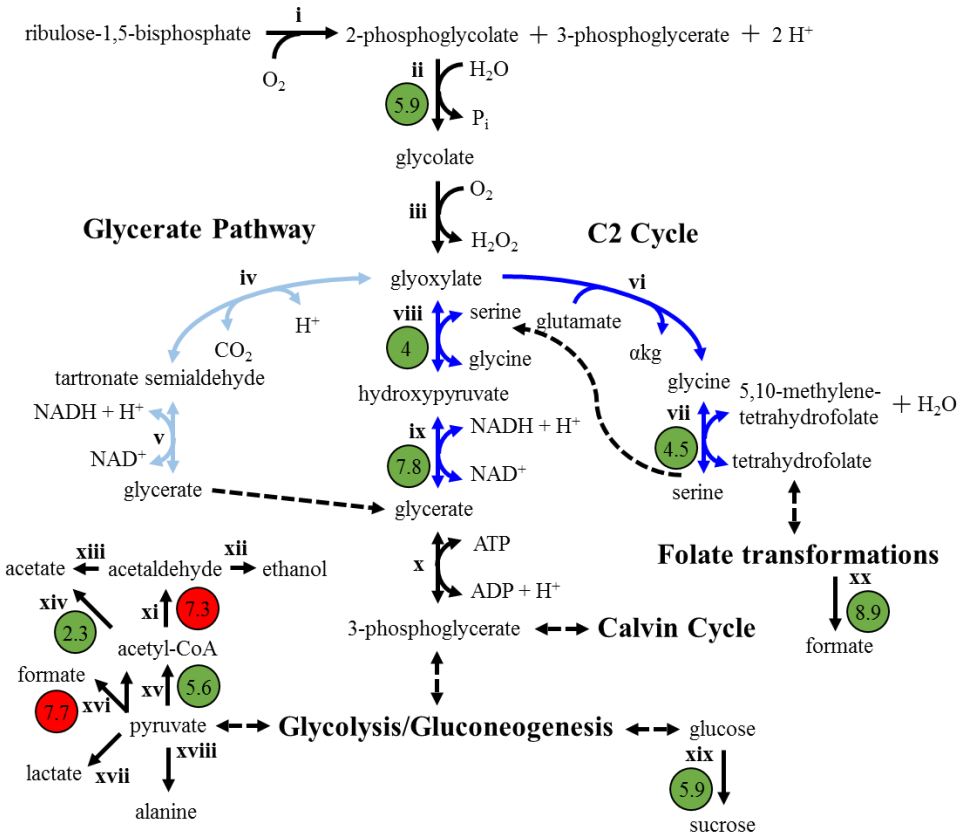

Figure 6. Cyanobacterium *T. elongatus* BP-1 photorespiration and byproduct secretion pathways with transcriptomic data measured under high versus low irradiance. Genome-based photorespiration routes (C2 cycle, dark blue, and glycerate pathway, light blue) and byproduct secretion pathways included in the BP-1 model are illustrated. Green circles represent upregulated gene expression measured under high irradiance (2000 versus 200 μmol photons m^{-2} s^{-1}), and red circles represent downregulated gene expression, previously measured in [33]. Numbers indicate fold change for each gene. Enzymes coded in Roman numerals are: i, ribulose-1,5-bisphosphate carboxylase oxygenase; ii, phosphoglycolate phosphatase; iii, glycolate oxidase; iv, glyoxylate carboligase; v, tartronate semialdehyde reductase; vi, glycine transaminase; vii, serine hydroxymethyltransferase; viii, serine-glyoxylate transaminase; ix, glycerate dehydrogenase; x, glycerate 3-kinase; xi, acetaldehyde dehydrogenase; xii, alcohol dehydrogenase; xiii, succinate-semialdehyde dehydrogenase; xiv, acetyl-CoA synthetase; xv, pyruvate dehydrogenase; xvi, formate acetyltransferase; xvii, lactate dehydrogenase; xviii, alanine dehydrogenase; xix, sucrose phosphate synthase and sucrose phosphate phosphatase; xx, formyltetrahydrofolate deformylase. Other abbreviations: αkg, α-ketoglutarate.

Finally, the transcriptomic data [33] showed upregulation of genes involved in both nitrate and sulfate uptake and assimilation under high irradiance conditions (Table A2 in Appendix C). Tradeoff curve analysis of the EFMs under high irradiance and O_2/CO_2 competition predicted increased use of the nitrate uptake reaction for strategies that secreted amino acids; conversely, no change in use of the sulfate uptake reaction was predicted. Reduction of nitrate to ammonia for amino acid synthesis represents an effective strategy for using excess electrons from the photosynthetic electron transport chain, consuming 8 moles of electrons per mole of nitrate reduced. Thus, at high irradiance and O_2 production, secretion of amino acids represents an economical stress acclimation strategy. Similarly, sulfate reduction also consumes 8 moles of electrons per mole of sulfate reduced to hydrogen sulfide,

which is used in synthesis of cysteine and methionine. Permitting secretion of cysteine or methionine in the computational model would lead to predictions of increased sulfate uptake. Altogether, comparison of the predicted competitive strategies with transcriptomic data under high irradiance (Table 3) suggests overall consistency of the computational model with photobioreactor observations.

3.5. Stress Acclimation and Photoautotrophic-Heterotrophic Interactions

BP-1 acclimation to a variety of culturing stresses was predicted to result in secretion of reduced carbon byproducts including organic acids and amino acids (Figures 3a and A2a,b; illustrated in Figure 7a). These byproducts represent a nutritional niche for heterotrophs. Photoautotrophic-heterotrophic cross-feeding could represent a mutually beneficial mechanism for buffering a photoautotroph from environmental stresses. Consumption of reduced carbon byproducts by the heterotroph would relieve potential inhibitory organic acid stress, as well as maximize the efficiency of total resource usage by the community (illustrated in Figure 7b). Cross-feeding of byproducts could also promote growth of the photoautotroph through consumption of O_2 by an aerobic heterotroph, thus decreasing local O_2 concentrations and lowering O_2/CO_2 competition. The amount of heterotroph able to be supported by secreted byproducts was predicted as a function of stress using published heterotrophic biomass per byproduct yields [76–82] (Figure 7c, see File S5 in the Supplementary Materials for calculations). The predicted amount of heterotrophic biomass that can be supported by BP-1 through cross-feeding of byproducts increased as stress increased due to higher byproduct yields at higher stress levels, as well as the varying heterotrophic biomass yields on different byproducts (Table A4 in Appendix C). The cross-feeding was also predicted to reduce local O_2 levels, which was calculated based on heterotrophic biomass O_2 requirements (Figure 7d, File S5 in the Supplementary Materials).

The predicted ratio of heterotroph to photoautotroph as a function of stress acclimation was compared to published photobioreactor co-culture data of BP-1 with the aerobic heterotroph *Meiothermus ruber* strain A [33]. Experiments reported heterotroph to photoautotroph ratios of ~1:10 [33]. This ratio, with some variation accounting for cell size differences between the two populations, falls within the range of heterotroph to photoautotroph ratios predicted at modest culturing stress (Figure 7c). These predictions considered autotrophic-heterotrophic interactions based on secreted carbon and not necessarily nitrogen source. Additional analysis of potential cross-feeding based on nitrogen or iron limitation can be found in Appendix B (Figure A2c–f).

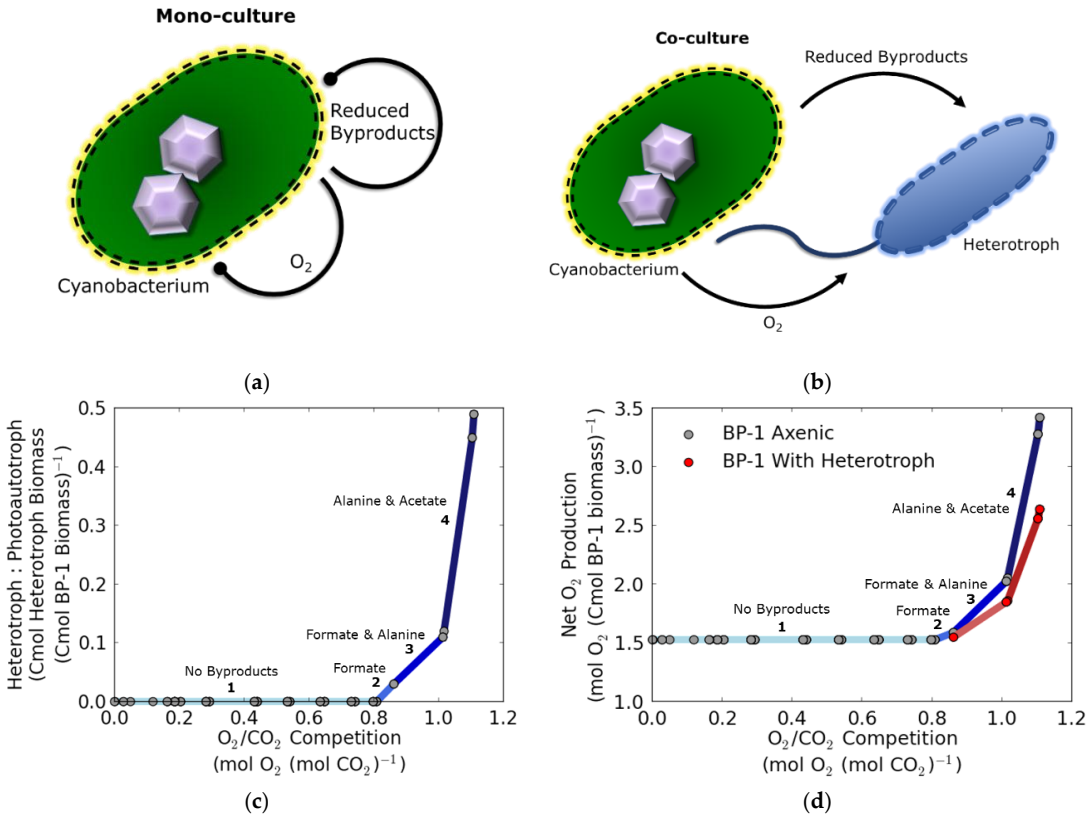

Figure 7. Byproduct secretion generates a heterotrophic niche and stimulates a mutually beneficial relationship. (**a**) Cyanobacterium BP-1 produces O_2 and reduced carbon compounds as metabolic byproducts during environmental stress, both of which are inhibitory to BP-1 growth. (**b**) The presence of reduced byproducts and O_2 forms a nutritional niche for heterotrophic organisms, which relieves inhibition for BP-1. (**c**) Heterotrophic biomass yield per BP-1 biomass (Cmol Cmol^{-1}) is presented as a function of O_2/CO_2 competition at RuBisCO (mol O_2 (mol CO_2)$^{-1}$ consumed) for the EFMs forming the optimal tradeoff with irradiance-induced stress. (**d**) Presence of a heterotroph lowers net O_2 production per Cmol BP-1 biomass as a function of O_2/CO_2 competition (mol O_2 (mol CO_2)$^{-1}$ consumed) for the EFMs forming the optimal tradeoff with irradiance-induced stress, which reduces O_2 inhibition. The distinct phenotypic regions defined by the tradeoff between O_2/CO_2 competition and irradiance-induced stress are labeled according to byproduct secretion patterns as in Figure 3a.

4. Discussion

Computational modeling was integrated with photobioreactor analyses to identify and interpret, from a systems perspective, the inferred mechanisms that underpin cyanobacterial acclimation to irradiance-associated stress. The combined results of this study show how different cyanobacterial systems, such as the photosynthetic apparatus and central carbon metabolism, can respond to environmentally induced stresses. Photobioreactor steady state growth of BP-1 showed decreased biomass production efficiency at high irradiance (Figure 4b), indicating that electrons were partitioned into non-biomass-producing alternative metabolic routes. Examination of transcriptomic data [33] comparing high to low irradiance conditions identified upregulation of genes involved in PSII operation, photorespiration, organic acid synthesis, and amino acid synthesis, among other pathways (Figure 6, Tables A2 and A3). Interrogation of BP-1 metabolic pathways with EFMA and resource allocation theory under conditions of high irradiance, high O_2, and limited nutrient availability provided a theoretical explanation for utilization of these pathways. Evolution has selected phenotypes which allocate limiting resources competitively. The origin of the stresses is the imbalance in resource acquisition which is manifested as a resource limitation. Acclimation to the resource stresses resulted

in the secretion of reduced byproducts in a behavior analogous to classic overflow metabolism in heterotrophs. The byproduct-secreting phenotypes represent a competitive and economical response to the stress [1]. It is worth noting that photobioreactor observations and computational predictions for BP-1 are in general agreement with the transcriptional patterns and physiological trends observed in the closely related *Synechococcus* sp. PCC 7002 [83]. The predicted byproduct secretion profiles furthermore control nutrient niches for proximal heterotrophic partners (Figure 7). In some cases, heterotrophic consumption of the byproducts represents a mutually beneficial interaction in that byproduct removal prevents accumulation of byproducts to a degree that represents an additional stress. This mutually beneficial interaction template likely plays a significant role in the many reported occurrences of photoautotrophic-heterotrophic consortia [84–86]. In fact, cross-feeding between BP-1 and the aerobic heterotroph *M. ruber* strain A has been both predicted by genome-scale modeling and observed in a laboratory setting [14,33].

The computational analyses investigated several metabolic acclimations to photosynthesis-associated stresses that apply broadly to photoautotrophs, including photosystem utilization and photorespiration strategies, the nature of reduced carbon byproducts, and the severity of O_2/CO_2 competition at RuBisCO. PSII was predicted to increase in photon absorption relative to PSI as irradiance increased (Figure 3), supported by transcriptomic data [33] (Tables 3 and A2). Increased relative photon absorption of PSII under higher irradiance is also reported in the literature from studies with the mesophilic cyanobacterium *Synechocystis* sp. PCC 6803 and is hypothesized to aid in reducing overall electron transport [68]. Additionally, increased utilization of the C2 photorespiration cycle at high irradiances may intersect with byproduct secretion strategies and contribute to amino acid synthesis as a resource-efficient strategy at high irradiances. Photorespiration permits salvage of carbon from unusable RuBisCO oxygenation byproducts; this carbon may be directed toward other byproduct pathways. The C2 photorespiration cycle requires more enzymatic steps and thus more biosynthetic resources (e.g., nitrogen) than the glycerate pathway, but links into glycine-serine interconversion and amino acid synthesis pathways.

Formate is the least reduced organic byproduct considered in the model (Table 1). It is predicted to be a more competitive byproduct secretion strategy at intermediate irradiance-induced stress and O_2/CO_2 competition, releasing a minimal quantity of electrons in the form of reduced carbon byproducts and retaining the remaining electrons for biomass (Figure 3). Alanine is predicted to be a competitive byproduct at high stress levels due to its high degree of reduction (Table 1). At high electron load (supported by high rates of oxygenic photosynthesis) and high O_2/CO_2 competition, alanine synthesis consumes more electrons per Cmol, resulting in a more efficient redox sink (Figure 3). Alanine was selected in this study as a representative amino acid; however, amino acids with higher nitrogen content, such as arginine, histidine, or lysine, would serve as even more effective electron sinks when nitrate is the nitrogen source. Genes involved in synthesis pathways for several amino acids beside alanine (Table A3 in Appendix C) were identified as upregulated under high irradiance conditions in the transcriptomic data [33]. Additionally, qualitative measurements from BP-1 steady state cultures have previously identified a variety of amino acids in the extracellular environment, including glutamate, isoleucine, leucine, lysine, phenylalanine, serine, threonine, and valine [33].

Experimental assessment of O_2/CO_2 competition and actual concentrations of O_2 and CO_2 at the active site of RuBisCO *in vivo* is challenging. The specificity factor, a kinetic constant describing the relative affinity of RuBisCO for CO_2 versus O_2 ($v_c/v_o = \mathrm{SF}[CO_2]/[O_2]$) [87], has been measured for a variety of phototrophs and is typically obtained from enzyme extracts. Falkowski and Raven [88] compiled a list of specificity factors from a variety of organisms, including cyanobacteria, algae, and plants, and estimated v_o/v_c ratios under assumptions of air equilibrium at 25 °C. These experimental estimates were compared with the predicted v_o/v_c values from the BP-1 model irradiance tradeoff curve (Figure 8a(A)). The variation in values within and among different types of organisms highlights the diversity of RuBisCO enzyme properties, which organisms are thought to have optimized over time based on different selective pressures [89,90]. However, the experimental estimates do not account for

the optimal temperature environment of the organism, the confounding influence of photosynthetic O_2 evolution, or effects of the carbon-concentrating mechanism, which may also be influenced by pH [91].

The specificity factor can be used to convert predicted O_2/CO_2 competition values to local relative O_2/CO_2 concentrations around RuBisCO [87], thereby permitting extension of stoichiometric modeling into the kinetic realm. Equivalent relative O_2/CO_2 competition values convert to different relative concentrations depending upon the magnitude of the specificity factor. Values for mesophilic cyanobacteria range from 45 to 70, and higher plants have an average value around 100 [87]. Figure 8a(B–D) shows the effect of varying the specificity factor on the O_2/CO_2 concentrations necessary to achieve the predicted v_o/v_c values along the irradiance tradeoff curve in Figure 3a; relative concentrations are lowered with a smaller specificity factor and raised with a higher specificity factor. A higher specificity factor indicates a greater tolerance to stress from O_2/CO_2 competition. *In vivo* measurements of oxygenation and carboxylation rates are sparse in the literature, particularly for microbial species; Taffs et al. [20] calculated a range of 3–7% oxygenation based on measurements of extracellularly secreted glycolate [92], but these values are likely an underestimate considering glycolate may be salvaged through the complete photorespiration pathway rather than excreted (Figure 3). Isotopic labeling studies of cyanobacteria also provide experimental data, but extrapolation of v_c/v_o ratios should be exercised with caution. Studies have shown operation of photorespiration even under high CO_2 (5%) conditions [93]. Another study has presented both modeling and experimental validation of the necessity of photorespiration even under saturating CO_2 conditions, positing that high CO_2 stimulates high photosynthetic rates to provide adequate energy for carbon fixation, which thereby leads to increased O_2 production levels [94]. Additionally, elevated temperatures have been shown to enhance oxygenation due to both changes in the specificity of RuBisCO and the different solubilities of O_2 and CO_2 [95] (Figure 8b). Experimental data on v_o/v_c. values is variable and dependent on the conditions under which the measurements were made. However, an environmental scenario with low O_2/CO_2 ratios may indicate that greater priority is placed on minimizing O_2/CO_2 competition than on minimizing photon absorption cost particularly under high irradiance conditions, e.g., O_2/CO_2 competition is a stronger driver of stress acclimation. Byproduct production and existence of heterotrophic partners is observed in experimental cyanobacterial systems, suggesting that byproduct production is an effective strategy for managing electrons from excess photon absorption. Instead, the cell may be simultaneously optimizing for other stresses such as biosynthetic nutrient investment like nitrogen or iron (Figure A2).

The systems-level analysis provided by this study indicated that the suite of metabolic carbon and electron sinks (i.e., secreted byproducts and biomass) is dependent upon environmental stressors. Pathway utilization and resource investments were co-dependent upon irradiance, O_2/CO_2 competition at RuBisCO, and DIC, nitrogen, and iron levels. These results provided novel insight into ecologically competitive metabolic strategies that cyanobacteria use to acclimate to environmental conditions. Physiological and transcriptomic [33] data paralleled the predictions, providing an additional level of support to the stoichiometric modeling predictions. It is noted that the stoichiometric model does not account for kinetic constraints, regulatory effects, or other aspects of thermodynamics beside reaction reversibilities [97,98], which may account for some of the differences between predictions and data and represents an avenue for further development. Finally, analysis of predicted optimal growth phenotypes was extended to make inferences about the nature of photoautotrophic-heterotrophic interactions and provide a theoretical basis for examining community composition. Taken holistically, this work presents a synergistic experimental and theoretical approach for understanding metabolic acclimation and provides a new level of insight into how different cyanobacterial systems, such as the photosynthetic apparatus and central carbon metabolism, coordinate and respond to environmental stresses that influence resource allocation.

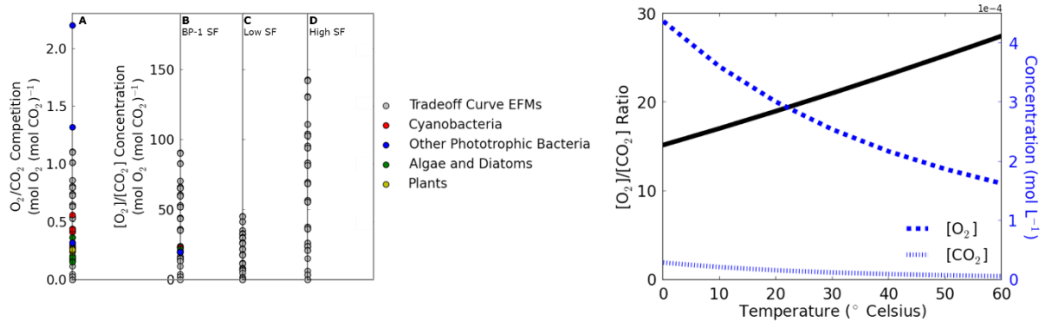

Figure 8. Comparison of computational and experimental O_2/CO_2 competition and concentrations at RuBisCO. (**a**) Predicted O_2/CO_2 competition values (mol O_2 (mol CO_2)$^{-1}$ consumed at RuBisCO) from the irradiance tradeoff curve in Figure 3a are shown in gray (**A**). Experimental O_2/CO_2 values for a variety of organisms calculated at air equilibrium and 25 °C [88] are overlaid in color. Predicted O_2/CO_2 competition values (gray points) were converted to relative O_2/CO_2 concentrations around RuBisCO by multiplying by the specificity factor (SF). The experimentally measured SF for BP-1 of 82 [87] was used for conversion in (**B**). Experimental data points from Falkowski and Raven (colored points) were converted to O_2/CO_2 concentrations via the respective SF of each organism [88]. Comparison of the BP-1 SF with lower and higher SF values is visualized using a lower SF of 41 (representative of *Synechococcus* sp.) (**C**) and a higher SF of 129 (representative of a red alga) (**D**). A lower SF indicates that lower relative O_2/CO_2 concentrations result in higher O_2/CO_2 competition ratios, whereas a higher SF indicates that an organism is more tolerant of higher relative O_2/CO_2 concentrations. (**b**) Temperature affects the relative propensity of RuBisCO for oxygenation. Dashed and dotted blue curves represent O_2 and CO_2 concentrations in aqueous phase at equilibrium with atmospheric concentrations, calculated using Henry's law constants from Sander [96]. The black curve represents the ratio of the $[O_2]$ to $[CO_2]$ curves, showing that the relative proportion of O_2 increases with elevated temperature. Calculations are provided in File S6.

Supplementary Materials: The following are available online at www.mdpi.com/2227-9717/5/2/32/s1, File S1: Model Reactions and Supporting Information, File S2: SBML Model Version, File S3: MATLAB Analysis Routines, File S4: Python Graphics Routines, File S5: Heterotroph Niche Calculations, File S6: Solubility Calculations.

Acknowledgments: This work is a contribution of the PNNL Foundational Scientific Focus Area (Principles of Microbial Community Design) subcontracted to Montana State University. Ashley E. Beck was supported by the Office of the Provost at Montana State University through the Molecular Biosciences Program and NSF (DMS-1361240). Hans C. Bernstein was supported by the Linus Pauling Distinguished Postdoctoral Fellowship which is a Laboratory Directed Research and Development program at PNNL, operated for the DOE by Battelle Memorial Institute under Contract DE-AC05-76RLO 1830. A portion of the research was performed using EMSL, a DOE Office of Science User Facility sponsored by BER under user proposal number 49356. The authors would like to acknowledge and thank Lye Meng Markillie, Eric Hill, Ryan McClure, and Margaret Romine for assisting with the culturing, RNA sequencing, and genome annotation activities that helped support this study and Reed Taffs for primary MATLAB algorithm development. The authors would also like to thank Kristopher Hunt, Zackary Jay, Heidi Schoen, Lee McGill, and William Moore for critical reading of the manuscript.

Author Contributions: A.E.B. and R.P.C. conceived and designed the experiments; A.E.B. and H.C.B. performed the experiments; A.E.B. analyzed the data; H.C.B. contributed reagents/materials/analysis tools; A.E.B. and R.P.C. wrote the manuscript.

Conflicts of Interest: The authors declare no conflict of interest. The funding sponsors had no role in the design of the study; in the collection, analyses, or interpretation of data; in the writing of the manuscript; and in the decision to publish the results.

Appendix A. Biomass Composition Analytical Methods

Appendix A.1. DNA, After Downs and Wilfinger [38]

50 µL of frozen cell pellet equivalent to approximately 1.5 mg of biomass (dry weight) was re-suspended in 50 µL of alkali extraction solution (1 N NH_4OH, 0.2% Triton X-100 with nuclease-free water) in 2-mL Eppendorf tubes. Tubes were incubated at 37 °C for 10 min in a block heater. After 10 min, samples were diluted to 2 mL total volume with assay buffer (100 mM NaCl, 10 mM EDTA, 10 mM Tris, pH 7.0 with HCl, nuclease-free water) and transferred to 15-mL Falcon tubes for centrifugation (2500× *g*, 30 min, 4 °C). Calf thymus DNA standards were prepared by making a DNA stock solution in nuclease-free water about 300 µg/mL (stored at 4 °C). Exact concentration was measured with a NanoDrop 1000 spectrophotometer. The standard solution was diluted to a working stock of 100 µg/mL with standard buffer (assay buffer containing the same concentration of alkali extraction solution as the diluted samples (100 mM NaCl, 10 mM EDTA, 10 mM Tris, pH 7.0 with HCl, 0.025 N NH_4OH, 0.005% Triton X-100)). The DNA working stock was then diluted into a standard series with standard buffer (1–5 µg/mL). 50 µL of sample or standard were added to a black polystyrene 96-well plate with clear bottom (Corning 3603). 295 µL of Hoechst working reagent was added to each well. Hoechst working reagent was prepared fresh daily from an intermediate stock of 200 µg/mL by diluting to 1 µg/mL with assay buffer. The intermediate stock was prepared from a 10 mg/mL stock solution by diluting to 200 µg/mL with nuclease-free water. Stock solutions and working stocks were stored at 4 °C wrapped in aluminum foil to protect from light. The wells were then read in a Synergy fluorescent plate reader using the following settings: (plate type) 96 well plate; (set temperature) setpoint 30 °C, preheat before moving to next step; (shake) double orbital 30 s, frequency 180 cpm; (read) fluorescence endpoint, 352 nm excitation, 461 nm emission, bottom optics, gain 100, Xenon flash light source, high lamp energy, normal read speed, 100 ms delay, 10 measurements/data point. Three reaction wells of sample or standard were performed for each sample or standard. The concentration of the samples was determined based on the average of the three standard calibration curves.

Appendix A.2. Glycogen, After Del Don et al. [39]

Anthrone reagent was prepared fresh daily according to Herbert et al. [99] and stored at 4 °C. Frozen cell pellet (−80 °C) was thawed and divided into three equal parts by mass in 2-mL Eppendorf tubes, approximately 0.5 mg dry weight. Each aliquot was re-suspended in 200 µL 2% sodium sulfate (*w*/*v*). Eppendorf tubes were sealed with parafilm and heated for 10 min at 70 °C in a block heater. After heating, 1 mL methanol was added to each tube and vortexed to co-precipitate glycogen and sodium sulfate. The precipitate was pelleted by centrifuging for 15 s at 10,000 rpm. The precipitate was washed with 1 mL methanol, until the pellet was white, to remove impurities. Pellets were then re-suspended in 1 mL reverse osmosis water and transferred to clean glass test tubes and placed on ice to chill. 5 mL of ice-cold anthrone reagent was added to each test tube. After adding reagent, tubes were chilled on ice for 5 min, vortexed gently to homogenize the solution, and transferred to a boiling water bath for 10 min. Tubes were then returned to ice for 5–10 min until cool, vortexed gently to mix contents, and absorbance at 625 nm was read with a Genysys spectrophotometer using a reagent blank. A glucose standard curve (10–190 µg/mL) was treated identically with anthrone reagent.

For total carbohydrate quantitation, the cell pellet aliquot was re-suspended in 1 mL reverse osmosis water and transferred to a clean glass test tube, and the anthrone procedure detailed above was followed. For quantitation of other cellular carbohydrates, the residual methanol from the extraction and washings were collected in an aluminum pan and evaporated, re-suspended in 1 mL reverse osmosis water, and the anthrone procedure detailed above was followed.

Appendix A.3. Lipid, After Bligh and Dyer [40]

Frozen cell pellet (10 mg) was re-suspended to 0.6 mL using Milli-Q water in a 15-mL polypropylene centrifuge tube. Chloroform (0.75 mL) and methanol (1.5 mL) were sequentially added, adhering to the 1:2:0.8 chloroform:methanol:water volume ratio recommended by Bligh and Dyer. The mixture was vortexed 15 min at speed setting 3 using a VWR vortex mixer. Chloroform (0.75 mL) and Milli-Q water (0.75 mL) were sequentially added, vortexing 10–15 seconds at speed setting 7 after each addition. Upon centrifugation (4000 rpm, 15 min, 20 °C), the lower chloroform phase, containing lipids, chlorophyll, and pigments, was transferred via micropipette to an aluminum pan that had been pre-dried at room temperature and pre-weighed. The liquid was evaporated in a fume hood and weighed at three different time intervals following evaporation. Weights were measured with a Mettler Toledo MT5 microbalance with accuracy to 0.001 mg and recorded as an average of three measurements. It was noted that chloroform may leach compounds from polypropylene materials; thus a blank reaction using 0.6 mL Milli-Q water was used and its weight was subtracted from the biological sample weight.

Appendix A.4. Protein and Amino Acid Distribution, After Henderson et al. [39]

Amount approximately equivalent to 3 mg of frozen cell pellet was transferred to borosilicate HPLC vials with PTFE/silicone caps. 50 µL 6 M HCl per mg biomass was added to each vial. The vials were tightly capped and hydrolyzed at 105 °C for 24 h using a block heater. After 24 h, the samples were then neutralized with 6 M NaOH to pH 7.0 and filtered with 0.22 µm PES spin filter in microfuge for 5 min at 10,000 rpm. Samples were then placed at −80 °C to freeze before lyophilizing for 24 h (VirTis benchtop lyophilizer). After lyophilization samples were placed at −80 °C until HPLC analysis. HPLC analysis was performed according to the following protocol validated and published by Agilent Technologies [41] using an Agilent 1100 HPLC equipped with fluorescence detector. Borate buffer was 0.4 N borate, pH 10.2 with NaOH; *o*-phthalaldehyde (OPA) reagent, 9-fluorenylmethylchloroformate (FMOC) reagent, and amino acid standards were obtained from Agilent. OPA and FMOC reagents were replaced daily in amber vials. Upon opening a vial of reagent, analyses were performed within 10 days. Solvent A was 40 mM sodium phosphate buffer (using 1:1 ratio of NaH_2PO_4 and Na_2HPO_4), pH 7.8 with NaOH, 0.2 µm filtered. Solvent B was 45:45:10 acetonitrile:methanol:water (*v*/*v*/*v*), 0.2 µm filtered. The pump rate was 1 mL/min, 47 min per injection, with gradient settings as follows:

Time (Min)	% Solvent B
0	0
3.8	0
36.2	57
37.2	100
44.6	100
46.4	0
47	0

The flow rate was halved and the timing was doubled from the procedure reported in the Agilent technical note to improve resolution and reduce wear on equipment. The column thermostat was set at 40 °C, and the autosampler thermostat was set at 4 °C. The fluorescence detector settings were as followed, to switch from OPA- to FMOC-derivatized amino acids:

Time (Min)	Ex/Em (nm)	PMT Gain
0	340/450	10
30	266/305	9

The injection program was as follows:

Step	Instruction
Step 1	Draw 2.5 µL from vial 1 (borate buffer)
Step 2	Draw 0.5 µL from sample
Step 3	Mix 3 µL in air, max speed, 2×
Step 4	Wait 0.5 min
Step 5	Draw 0 µL from vial 2 (needle wash)
Step 6	Draw 0.5 µL from vial 3 (OPA)
Step 7	Mix 3.5 µL in air, max speed, 6×
Step 8	Draw 0 µL from vial 2 (needle wash)
Step 9	Draw 0.5 µL from vial 4 (FMOC)
Step 10	Mix 4 µL in air, max speed, 6×
Step 11	Draw 32 µL from vial 5 (water)
Step 12	Mix 18 µL in air, max speed, 2×
Step 13	Inject
Auxiliary settings	Drawspeed = 200 µL/min
	Ejectspeed = 600 µL/min
	Draw position = 0.0 mm

The integration parameters for collecting the data were set according to the following parameters.

Parameter	Value
Slope Sensitivity	1
Peak Width	0.04
Area Reject	1
Height Reject	0.4
Shoulders	OFF

Appendix A.5. RNA, After Benthin et al. *[43]*

Samples were thawed and washed three times with 3 mL 0.7 M $HClO_4$ for degradation of cell walls, vortexing to re-suspend in between washing and centrifuging at 4000 rpm for 10 min at 4 °C. The pellet was then re-suspended in 3 mL 0.3 M KOH to lyse the cells and was incubated in a 37 °C water bath for 1 h, shaking at 15-min intervals. After 1 h, samples were cooled and 1 mL 3 M $HClO_4$ was added for neutralization. The solution was centrifuged at the same specifications as before, and the supernatant was poured off into a new centrifuge tube. The pellet was washed twice with 4 mL 0.5 M $HClO_4$, centrifuged, and supernatant added to the new tube. 0.5 M $HClO_4$ extracts the RNA, while DNA, which is stable even in strong alkali, and protein, which does not solubilize in the alkali, remain in the precipitate. The collection of extracts was made up to a volume of 15 mL by adding 3 mL 0.5 M $HClO_4$ and was centrifuged once more to remove any non-visible precipitates of $KClO_4$. Upon final centrifugation, absorbance was measured at 260 nm against a 0.5 M $HClO_4$ blank using disposable UV cuvettes rated to 220 nm. Linearity of the spectrophotometer was confirmed within that range by successively diluting the sample twice with 0.5 M $HClO_4$ and confirming a linear fit to the three measured absorbances at 260 nm. Calculation of RNA quantity was performed by assuming 1 unit of absorbance at 260 nm corresponds to 38 µg/mL RNA on average [100].

Appendix B. Supplemental Figures

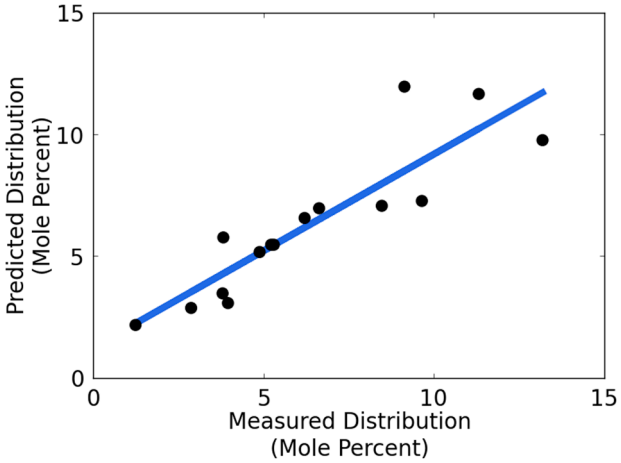

Figure A1. BP-1 amino acid distribution. Correlation between the predicted amino acid distribution (based on protein-coding gene sequences) and the experimentally measured distribution. Cysteine, methionine, and tryptophan are excluded from the correlation due to degradation during hydrolysis of the biomass samples to extract the protein. The equation of the best-fit linear trendline is $y = 0.79x + 1.29$ with $R^2 = 0.79$.

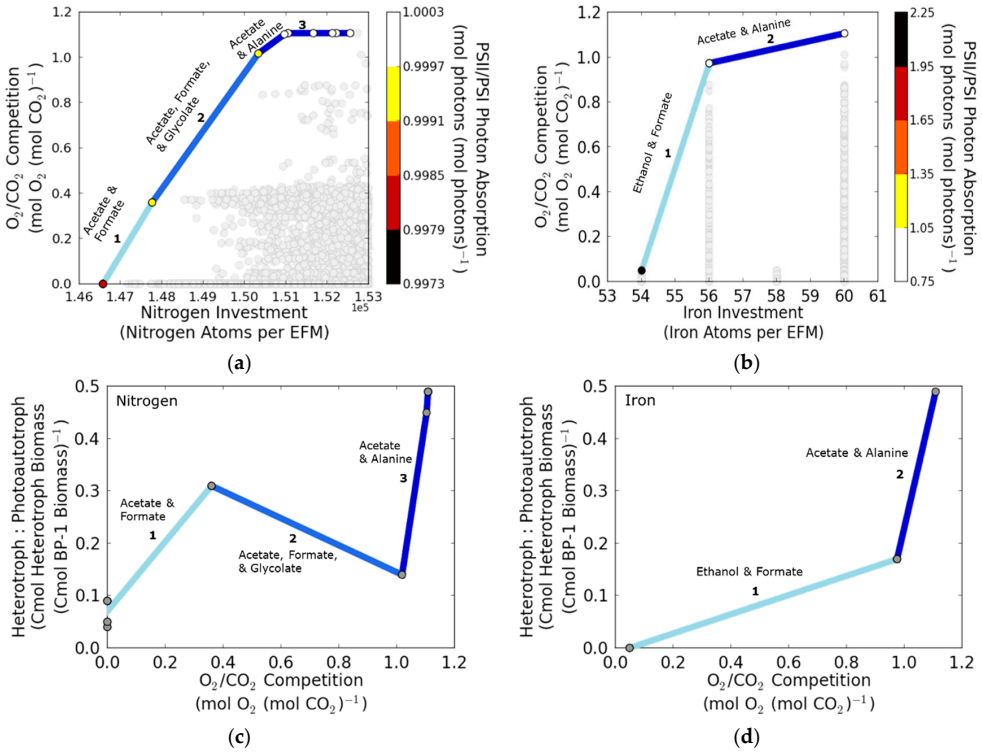

Figure A2. *Cont.*

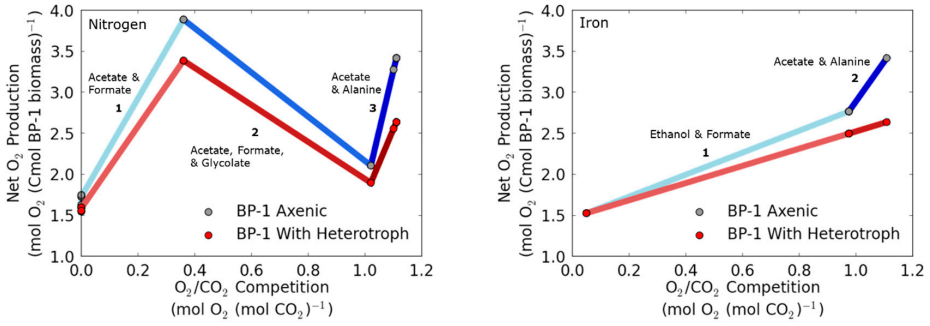

Figure A2. Computational analysis of nutrient availability and O_2/CO_2 competition at RuBisCO in cyanobacterium BP-1. (**a**) Nitrogen availability. O_2/CO_2 competition (mol O_2 (mol CO_2)$^{-1}$ consumed at RuBisCO) as a function of nitrogen investment (nitrogen atoms per EFM) for biomass-producing EFMs. The tradeoff curve defining competitive strategies between O_2/CO_2 competition and nitrogen limitation was divided into three distinct phenotypic regions based on byproduct secretion, labeled accordingly (intensity of shading increases with increasing stress levels). Points in the plot area are representative of 1,430,252 EFMs. (**b**) Iron availability. O_2/CO_2 competition (mol O_2 (mol CO_2)$^{-1}$ consumed at RuBisCO) as a function of iron investment (iron atoms per EFM, considering only photosynthetic and central metabolism reactions) for biomass-producing EFMs. The tradeoff curve defining competitive strategies between O_2/CO_2 competition and iron limitation was divided into two distinct phenotypic regions based on byproduct secretion, labeled accordingly (intensity of shading increases with increasing stress levels). Color scale represents the photon absorption at PSII relative to PSI for EFMs on the tradeoff curve (mol photons absorbed at PSII (mol photons absorbed at PSI)$^{-1}$). Each point represents a unique EFM. Modeled biomass production did not include maintenance energy requirements. Points in the plot area are representative of 4,615,500 EFMs. (**c**,**d**) Heterotrophic biomass yield per BP-1 biomass (Cmol Cmol^{-1}) is presented as a function of O_2/CO_2 competition at RuBisCO (mol O_2 (mol CO_2)$^{-1}$ consumed) for the EFMs forming the optimal tradeoffs with nitrogen and iron availability, respectively. (**e**,**f**) Presence of a heterotroph lowers net O_2 production per Cmol BP-1 biomass as a function of O_2/CO_2 competition (mol O_2 (mol CO_2)$^{-1}$ consumed) for the EFMs forming the optimal tradeoffs with nitrogen and iron availability, respectively, which reduces O_2 inhibition. The distinct phenotypic regions defined by the tradeoff between O_2/CO_2 competition and nutrient availability stress are labeled according to byproduct secretion patterns as in panels (**a**,**b**).

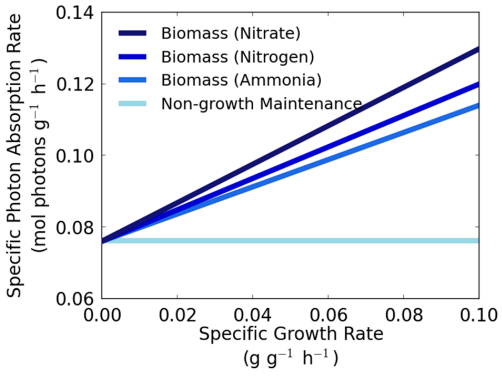

Figure A3. Analysis of influence of nitrogen source on photon requirement. Comparison of the impact of various nitrogen sources on the theoretical specific photon absorption rate necessary for biomass production. Photon absorption rates (mol photons absorbed (g CDW)$^{-1}$ h^{-1}) were calculated using the BP-1 experimentally measured biomass composition. Ammonia is a completely reduced form of nitrogen, whereas and molecular nitrogen and nitrate are less reduced forms and require successively more energy for reduction to be assimilated into biomass, causing an increase in the specific photon absorption rate. Nitrate serves as the most effective sink for excess electrons from the photosynthetic electron transport chain.

Appendix C. Supplemental Tables

Table A1. Experimentally measured amino acid distribution from OPA/FMOC derivatization and HPLC fluorescence detection. Amino acids are abbreviated according to IUPAC 1-letter convention; average mole percent of two separately hydrolyzed samples and percent relative standard deviation are reported.

Amino Acid	Mole %	% RSD
Q/E	13.1	0.16
N/D	10.1	0.07
L	9.4	0.08
A	9.2	0.24
R	8.5	0.96
V	6.1	0.97
I	5.4	0.29
G	5.0	0.02
F	4.9	0.15
T	4.9	0.07
K	4.5	1.96
Y	4.1	0.01
S	4.0	0.08
P	3.4	1.21
H	1.5	0.14

Table A2. Upregulated BP-1 genes under high versus low irradiance conditions (2000 versus 200 µmol photons m^{-2} s^{-1}) [33] involved in photosystem II (PSII), carbon-concentrating mechanism (CCM), Calvin cycle carbon fixation, glycolysis, TCA cycle, oxidative phosphorylation (OP), and nitrate and sulfate uptake and assimilation. For each pathway, upregulated genes are listed in the left column with corresponding fold change in the right column.

PSII		CCM		Calvin		Glycolysis	
psbA3	42.0	*ccmK1*	2.5	*gap2*	5.3	*eno*	4.6
psbP	4.3	*ccmK2*	2.1	*gapA*	4.5	*gap2*	5.3
psbX	3.3	*ccmK3*	2.6	*glpX*	6.6	*gapA*	4.5
psbQ	2.7	*ccmM*	2.5	*pgk*	2.1	*gmpA*	6.4
psb29	2.6	*tlr0311*	2.4	*prkB*	13.4	*gpmI*	5.4
psb32	4.1			*rpiA*	16.2	*pfkA*	2.3
				tpiA	5.2	*pgk*	2.1
						pyk	3.5
						tpiA	5.2
TCA		**OP**		**Nitrate**		**Sulfate**	
acnB	2.2	*atpC*	2.2	*narM*	2.3	*cysA*	2.5
fumC	3.2	*atpD*	5.2	*nirA*	3.4	*cysC1*	3.9
gltA	4.7	*atpE*	2.2	*ntcB*	4.9	*cysH*	4.6
idh3	6.3	*atpF*	2.9	*nrtA*	2.2	*cysQ*	3.1
sdhC	2.0	*atpG*	3.2	*nrtD*	2.5	*met3*	8.5
		atpH	2.8	*tll1357*	3.1		
		cydB	3.6				
		ndh	2.0				
		ndhA	6.3				
		ndhB	4.4				
		ndhC	6.1				
		ndhD3	13.2				
		ndhE	4.7				
		ndhF3	2.4				
		ndhG	3.0				
		ndhH	2.2				
		ndhI	4.9				
		ndhJ	6.6				
		ndhK	3.1				
		ndhL	4.9				
		ndhM	13.1				
		ndhN	9.8				
		ppa	3.6				
		sdhC	2.0				

Table A3. Genes involved in amino acid synthesis pathways found to be upregulated under high irradiance conditions (2000 versus 200 µmol photons m^{-2} s^{-1}) [33]. Amino acids are abbreviated according to IUPAC 1-letter convention and number of nitrogen atoms follows in parentheses. For each amino acid, upregulated genes are listed in the left column with corresponding fold change in the right column.

R (4)		N/D (2/1)		C (1)		Q (2)		H (3)		I/L/V (1/1/1)		K (2)		M (1)		F/W/Y (1/2/1)		P (1)		S (1)		T (1)		Transporters	
argB	3.0	*asnB*	2.5	*cysE*	4.0	*glnA*	3.6	*hisA*	3.4	*avtA*	2.8	*dapA*	2.9	*metE*	12.9	*aroA*	9.2	*proB*	6.7	*glyA*	4.5	*thrA*	2.6	*tlr1046*	2.2
argC	4.8	*ansA2*	3.0					*hisB*	3.9	*cimA*	2.5	*dapB*	4.5			*aroB*	4.3			*serA*	7.8	*thrB1*	3.7	*tlr1067*	3.4
argD	2.5	*aspB*	2.7					*hisIE*	6.7	*ilvE*	5.6	*dapF*	4.1			*aroC*	4.3					*thrCII*	6.3	*tll1105*	2.4
argG	14.0							*hisG*	2.3	*leuB*	6.0	*dapL1*	4.0			*aroE*	2.4							*tlr1120*	16.5
argH	4.4							*hisF*	2.0	*leuC*	2.9	*lysA*	3.3			*trpA*	2.6							*tlr1121*	3.6
argJ	4.0											*lysC*	2.1			*trpB*	2.5							*tlr1151*	2.3
																trpC	2.2							*tll1318*	2.7
																trpE	4.1							*tlr1592*	2.1
																trpF	2.3								
																tyrAa	2.4								

Table A4. Byproduct yields with respect to BP-1 biomass for pathways that secreted byproducts along the tradeoff curve for irradiance-induced stress and O_2/CO_2 competition and the corresponding yield of heterotroph biomass. Heterotroph yield was obtained via substrate consumption costs estimated from the literature for the respective byproducts (Cmol per Cmol heterotroph biomass): 4.53 for formate [77], 2.66 for alanine [78], and 2.61 for acetate [76]. Photons absorbed per BP-1 are reported in mol $Cmol^{-1}$, O_2/CO_2 competition is reported in mol mol^{-1}, and yields are reported in Cmol $Cmol^{-1}$.

Photons Absorbed Per BP-1 Biomass	O_2/CO_2 Competition	Formate Per BP-1 Biomass	Alanine Per BP-1 Biomass	Acetate Per BP-1 Biomass	Heterotroph Biomass Per BP-1 Biomass
33.26	0.86	0.13	NA	NA	0.03
51.36	1.01	NA	0.30	NA	0.11
52.44	1.02	NA	0.31	0.01	0.12
100.05	1.10	NA	0.84	0.36	0.45
105.55	1.11	NA	0.90	0.40	0.49

Appendix D. Nitrogen and Iron Limitation

Nitrogen is a major component of protein but is often scarce in the environment [101]. Ecologically competitive acclimation to increased O_2/CO_2 competition as a function of pathway nitrogen requirement is shown in Figure A2a in Appendix B; the tradeoff surface defines three phenotypic regions according to byproduct secretion. The EFM at the lower left corner of the plot represents nitrogen-limited cyanobacterial growth under low O_2/CO_2 competition; byproduct secretion is predicted even at the lowest nitrogen stress. With increasing O_2/CO_2 competition and nitrogen investment, BP-1 is predicted to secrete a number of reduced carbon compounds along the tradeoff surface, including acetate, formate, glycolate, and under the highest stress, the amino acid alanine. Production of byproducts is predicted to achieve the most efficient nitrogen utilization while simultaneously minimizing O_2/CO_2 competition. EFMs on the nitrogen tradeoff surface exclusively use the C2 photorespiration cycle whereas the glycerate pathway is not used (Figure A2a in Appendix B), similar to the result for irradiance-induced stress in Figure 3a. Also similar to the result for irradiance-induced stress, relative PSII/PSI photon absorption increases along the tradeoff surface, with greater relative photon absorption at PSII at higher O_2/CO_2 competition and higher nitrogen investment (Figure A2a in Appendix B).

Biologically available iron is often limiting in microbial habitats due to low solubility, which is exacerbated at elevated pH [102]. Figure A2b in Appendix B predicts acclimation to increased O_2/CO_2 competition as a function of pathway iron investment. Two phenotypic regions of byproduct secretion were defined by the tradeoff surface, including combinations of ethanol, formate, and acetate, and finally alanine under the highest stress. Under low iron, relative PSII/PSI photon absorption decreases along the tradeoff surface as O_2/CO_2 competition and iron investment increase, showing a reversed trend compared with irradiance-induced stress and nitrogen investment. Analogous to the result for irradiance-induced stress in Figure 3a, the C2 cycle is the predominant photorespiration strategy as O_2/CO_2 competition increases. At low O_2/CO_2 competition, the relative PSII/PSI photon absorption is nearly twice that at high O_2/CO_2 competition (the scale shows greater variability than the scale for light stress or nitrogen investment in Figures 3a and A3a) and again indicates higher gross O_2 and ATP production. Additionally, as compared to the tradeoff surface in Figure 3a, the responses to nitrogen and iron limitation are less robust; fewer suboptimal pathways exist in close proximity to the tradeoff surface.

Appendix E. Biomass Yield Comparison

The physiological light response experiments allowed for comparison of photon costs for synthesizing BP-1 biomass with results reported in previously published studies for *Cyanothece* sp. ATCC 51142 and the green alga *Chlamydomonas reinhardtii* [30,103]. This comparison is of interest because experimental photon requirement values are relatively uncommon. The photon cost per biomass for BP-1 was about three times higher than the costs for these two organisms. This result may be due to the thermophilic nature of the organism and/or higher maintenance costs incurred by alkaline habitats. The nonlinear increase observed in the overall experimental photon absorption rate as growth rate increases (Figure 5) may correspond to increased cellular stress with higher maintenance energy requirements or greater thermal dissipation at higher irradiances. For example, higher irradiance may necessitate increased repair of photosystem proteins or a greater proportion of light may be lost to inefficiency [88]. These experiments and simulations demonstrate the wide range of irradiances under which BP-1 is capable of growing, stimulating interest in the metabolic strategies microbes such as this thermophilic cyanobacterium use to manage the daily fluctuations in irradiance and the accompanying stresses.

References

1. Folsom, J.P.; Carlson, R.P. Physiological, biomass elemental composition and proteomic analyses of *Escherichia coli* ammonium-limited chemostat growth, and comparison with iron- and glucose-limited chemostat growth. *Microbiology* **2015**, *161*, 1659–1670. [CrossRef] [PubMed]
2. Schimel, J.; Balser, T.C.; Wallenstein, M. Microbial stress-response physiology and its implications for ecosystem function. *Ecology* **2007**, *88*, 1386–1394. [CrossRef] [PubMed]
3. Rousseaux, C.S.; Gregg, W.W. Interannual variation in phytoplankton primary production at a global scale. *Remote Sens.* **2014**, *6*, 1–19. [CrossRef]
4. Bullerjahn, G.S.; Post, A.F. Physiology and molecular biology of aquatic cyanobacteria. *Front. Microbiol.* **2014**, *5*. [CrossRef] [PubMed]
5. Abed, R.M.M.; Dobretsov, S.; Sudesh, K. Applications of cyanobacteria in biotechnology. *J. Appl. Microbiol.* **2009**, *106*, 1–12. [CrossRef] [PubMed]
6. Singh, S.; Kate, B.N.; Banerjee, U.C. Bioactive compounds from cyanobacteria and microalgae: An overview. *Crit. Rev. Biotechnol.* **2005**, *25*, 73–95. [CrossRef] [PubMed]
7. Raven, J.A. The cost of photoinhibition. *Physiol. Plant.* **2011**, *142*, 87–104. [CrossRef] [PubMed]
8. Bailey, S.; Grossman, A. Photoprotection in cyanobacteria: Regulation of light harvesting. *Photochem. Photobiol.* **2008**, *84*, 1410–1420. [CrossRef] [PubMed]
9. Bernstein, H.C.; Kesaano, M.; Moll, K.; Smith, T.; Gerlach, R.; Carlson, R.P.; Miller, C.D.; Peyton, B.M.; Cooksey, K.E.; Gardner, R.D.; et al. Direct measurement and characterization of active photosynthesis zones inside wastewater remediating and biofuel producing microalgal biofilms. *Bioresour. Technol.* **2014**, *156*, 206–215. [CrossRef] [PubMed]
10. Ward, D.M.; Bateson, M.M.; Ferris, M.J.; Kuhl, M.; Wieland, A.; Koeppel, A.; Cohan, F.M. Cyanobacterial ecotypes in the microbial mat community of Mushroom Spring (Yellowstone National Park, Wyoming) as species-like units linking microbial community composition, structure and function. *Philos. Trans. R. Soc. B* **2006**, *361*, 1997–2008. [CrossRef] [PubMed]
11. Eisenhut, M.; Ruth, W.; Haimovich, M.; Bauwe, H.; Kaplan, A.; Hagemann, M. The photorespiratory glycolate metabolism is essential for cyanobacteria and might have been conveyed endosymbiontically to plants. *Proc. Natl. Acad. Sci. USA* **2008**, *105*, 17199–17204. [CrossRef] [PubMed]
12. Espie, G.S.; Kimber, M.S. Carboxysomes: Cyanobacterial rubisco comes in small packages. *Photosynth. Res.* **2011**, *109*, 7–20. [CrossRef] [PubMed]
13. Rae, B.D.; Long, B.M.; Whitehead, L.F.; Forster, B.; Badger, M.R.; Price, G.D. Cyanobacterial carboxysomes: Microcompartments that facilitate CO_2 fixation. *J. Mol. Microbiol. Biotechnol.* **2013**, *23*, 300–307. [CrossRef] [PubMed]
14. Henry, C.S.; Bernstein, H.C.; Weisenhorn, P.; Taylor, R.C.; Lee, J.Y.; Zucker, J.; Song, H.S. Microbial community metabolic modeling: A community data-driven network reconstruction. *J. Cell. Physiol.* **2016**, *231*, 2339–2345. [CrossRef] [PubMed]
15. Llaneras, F.; Pico, J. Stoichiometric modelling of cell metabolism. *J. Biosci. Bioeng.* **2008**, *105*, 1–11. [CrossRef] [PubMed]
16. Maarleveld, T.R.; Khandelwal, R.A.; Olivier, B.G.; Teusink, B.; Bruggeman, F.J. Basic concepts and principles of stoichiometric modeling of metabolic networks. *Biotechnol. J.* **2013**, *8*, 997–1008. [CrossRef] [PubMed]
17. Orth, J.D.; Thiele, I.; Palsson, B.O. What is flux balance analysis? *Nat. Biotechnol.* **2010**, *28*, 245–248. [CrossRef] [PubMed]
18. Perez-Garcia, O.; Lear, G.; Singhal, N. Metabolic network modeling of microbial interactions in natural and engineered environmental systems. *Front. Microbiol.* **2016**, *7*. [CrossRef] [PubMed]
19. Trinh, C.T.; Wlaschin, A.; Srienc, F. Elementary mode analysis: A useful metabolic pathway analysis tool for characterizing cellular metabolism. *Appl. Microbiol. Biotechnol.* **2009**, *81*, 813–826. [CrossRef] [PubMed]
20. Taffs, R.; Aston, J.E.; Brileya, K.; Jay, Z.; Klatt, C.G.; McGlynn, S.; Mallette, N.; Montross, S.; Gerlach, R.; Inskeep, W.P.; et al. In silico approaches to study mass and energy flows in microbial consortia: A syntrophic case study. *BMC Syst. Biol.* **2009**, *3*, 114. [CrossRef] [PubMed]
21. Schuster, S.; Hilgetag, C. On elementary flux modes in biochemical reaction systems at steady state. *J. Biol. Syst.* **1994**, *2*, 165–182. [CrossRef]

22. Beck, A.E.; Hunt, K.A.; Bernstein, H.C.; Carlson, R.P. Interpreting and designing microbial communities for bioprocess applications, from components to interactions to emergent properties. In *Biotechnology for Biofuel Production and Optimization*; Eckert, C.E., Trinh, C.T., Eds.; Elsevier: Amsterdam, The Netherlands, 2016; pp. 407–432.
23. Carlson, R.P. Decomposition of complex microbial behaviors into resource-based stress responses. *Bioinformatics* **2009**, *25*, 90–97. [CrossRef] [PubMed]
24. Carlson, R.P.; Oshota, O.J.; Taffs, R.L. Systems analysis of microbial adaptations to simultaneous stresses. In *Reprogramming Microbial Metabolic Pathways*; Wang, X., Chen, J., Quinn, P., Eds.; Springer: Dordrecht, The Netherlands, 2012; pp. 139–157.
25. Molenaar, D.; van Berlo, R.; de Ridder, D.; Teusink, B. Shifts in growth strategies reflect tradeoffs in cellular economics. *Mol. Syst. Biol.* **2009**, *5*. [CrossRef] [PubMed]
26. Mori, M.; Hwa, T.; Martin, O.C.; De Martino, A.; Marinari, E. Constrained allocation flux balance analysis. *PLoS Comput. Biol.* **2016**, *12*, e1004913. [CrossRef] [PubMed]
27. Knoop, H.; Grundel, M.; Zilliges, Y.; Lehmann, R.; Hoffmann, S.; Lockau, W.; Steuer, R. Flux balance analysis of cyanobacterial metabolism: The metabolic network of *Synechocystis* sp. PCC 6803. *PLoS Comput. Biol.* **2013**, *9*, e1003081. [CrossRef] [PubMed]
28. Nogales, J.; Gudmundsson, S.; Knight, E.M.; Palsson, B.O.; Thiele, I. Detailing the optimality of photosynthesis in cyanobacteria through systems biology analysis. *Proc. Natl. Acad. Sci. USA* **2012**, *109*, 2678–2683. [CrossRef] [PubMed]
29. Vu, T.T.; Hill, E.A.; Kucek, L.A.; Konopka, A.E.; Beliaev, A.S.; Reed, J.L. Computational evaluation of *Synechococcus* sp. PCC 7002 metabolism for chemical production. *Biotechnol. J.* **2013**, *8*, 619–630. [CrossRef] [PubMed]
30. Vu, T.T.; Stolyar, S.M.; Pinchuk, G.E.; Hill, E.A.; Kucek, L.A.; Brown, R.N.; Lipton, M.S.; Osterman, A.; Fredrickson, J.K.; Konopka, A.E.; et al. Genome-scale modeling of light-driven reductant partitioning and carbon fluxes in diazotrophic unicellular cyanobacterium *Cyanothece* sp. ATCC 51142. *PLoS Comput. Biol.* **2012**, *8*, e1002460. [CrossRef] [PubMed]
31. Everroad, R.C.; Otaki, H.; Matsuura, K.; Haruta, S. Diversification of bacterial community composition along a temperature gradient at a thermal spring. *Microbes Environ.* **2012**, *27*, 374–381. [CrossRef] [PubMed]
32. Yamaoka, T.; Satoh, K.; Katoh, S. Photosynthetic activities of a thermophilic blue-green-alga. *Plant Cell Physiol.* **1978**, *19*, 943–954. [CrossRef]
33. Bernstein, H.C.; McClure, R.S.; Thiel, V.; Sadler, N.C.; Kim, Y.M.; Chrisler, W.B.; Hill, E.A.; Bryant, D.A.; Romine, M.F.; Jansson, J.K.; et al. Indirect interspecies regulation; transcriptional and physiological responses of a cyanobacterium to heterotrophic partnership. *mSystems* **2017**, *2*. [CrossRef] [PubMed]
34. Stanier, R.Y.; Kunisawa, R.; Mandel, M.; Cohen-Bazire, G. Purification and properties of unicellular blue-green algae (order Chroococcales). *Bacteriol. Rev.* **1971**, *35*, 171–205. [PubMed]
35. Bernstein, H.C.; Konopka, A.; Melnicki, M.R.; Hill, E.A.; Kucek, L.A.; Zhang, S.Y.; Shen, G.Z.; Bryant, D.A.; Beliaev, A.S. Effect of mono- and dichromatic light quality on growth rates and photosynthetic performance of *Synechococcus* sp. PCC 7002. *Front. Microbiol.* **2014**, *5*. [CrossRef] [PubMed]
36. Melnicki, M.R.; Pinchuk, G.E.; Hill, E.A.; Kucek, L.A.; Stolyar, S.M.; Fredrickson, J.K.; Konopka, A.E.; Beliaev, A.S. Feedback-controlled led photobioreactor for photophysiological studies of cyanobacteria. *Bioresour. Technol.* **2013**, *134*, 127–133. [CrossRef] [PubMed]
37. Shibata, K.; Benson, A.A.; Calvin, M. The absorption spectra of suspensions of living micro-organisms. *Biochim. Biophys. Acta* **1954**, *15*, 461–470. [CrossRef]
38. Downs, T.R.; Wilfinger, W.W. Fluorometric quantification of DNA in cells and tissue. *Anal. Biochem.* **1983**, *131*, 538–547. [CrossRef]
39. Del Don, C.; Hanselmann, K.W.; Peduzzi, R.; Bachofen, R. Biomass composition and methods for the determination of metabolic reserve polymers in phototrophic sulfur bacteria. *Aquat. Sci.* **1994**, *56*, 1–15. [CrossRef]
40. Bligh, E.G.; Dyer, W.J. A rapid method of total lipid extraction and purification. *Can. J. Biochem. Physiol.* **1959**, *37*, 911–917. [CrossRef] [PubMed]
41. Henderson, J.W.; Ricker, R.D.; Bidlingmeyer, B.A.; Woodward, C. *Rapid, Accurate, Sensitive, and Reproducible HPLC Analysis of Amino Acids*; Agilent Technologies: Santa Clara, CA, USA, 2000.

42. Fountoulakis, M.; Lahm, H.W. Hydrolysis and amino acid composition analysis of proteins. *J. Chromatogr. A* **1998**, *826*, 109–134. [CrossRef]
43. Benthin, S.; Nielsen, J.; Villadsen, J. A simple and reliable method for the determination of cellular RNA-content. *Biotechnol. Tech.* **1991**, *5*, 39–42. [CrossRef]
44. Klamt, S.; Saez-Rodriguez, J.; Gilles, E.D. Structural and functional analysis of cellular networks with CellNetAnalyzer. *BMC Syst. Biol.* **2007**, *1*. [CrossRef] [PubMed]
45. Klamt, S.; von Kamp, A. An application programming interface for CellNetAnalyzer. *Biosystems* **2011**, *105*, 162–168. [CrossRef] [PubMed]
46. Nakamura, Y.; Kaneko, T.; Sato, S.; Ikeuchi, M.; Katoh, H.; Sasamoto, S.; Watanabe, A.; Iriguchi, M.; Kawashima, K.; Kimura, T.; et al. Complete genome structure of the thermophilic cyanobacterium *Thermosynechococcus elongatus* BP-1. *DNA Res.* **2002**, *9*, 123–130. [CrossRef] [PubMed]
47. Caspi, R.; Billington, R.; Ferrer, L.; Foerster, H.; Fulcher, C.A.; Keseler, I.M.; Kothari, A.; Krummenacker, M.; Latendresse, M.; Mueller, L.A.; et al. The MetaCyc database of metabolic pathways and enzymes and the BioCyc collection of pathway/genome databases. *Nucleic Acids Res.* **2016**, *44*, D471–D480. [CrossRef] [PubMed]
48. Kanehisa, M.; Goto, S.; Sato, Y.; Furumichi, M.; Tanabe, M. KEGG for integration and interpretation of large-scale molecular data sets. *Nucleic Acids Res.* **2012**, *40*, D109–D114. [CrossRef] [PubMed]
49. Schomburg, I.; Chang, A.; Placzek, S.; Sohngen, C.; Rother, M.; Lang, M.; Munaretto, C.; Ulas, S.; Stelzer, M.; Grote, A.; et al. BRENDA in 2013: Integrated reactions, kinetic data, enzyme function data, improved disease classification: New options and contents in BRENDA. *Nucleic Acids Res.* **2013**, *41*, D764–D772. [CrossRef] [PubMed]
50. Beck, C.; Knoop, H.; Axmann, I.M.; Steuer, R. The diversity of cyanobacterial metabolism: Genome analysis of multiple phototrophic microorganisms. *BMC Genom.* **2012**, *13*, 56. [CrossRef] [PubMed]
51. Neidhardt, F.C.; Ingraham, J.L.; Schaechter, M. *Physiology of the Bacterial Cell: A Molecular Approach*; Sinauer Associates: Sunderland, MA, USA, 1990.
52. Maslova, I.P.; Mouradyan, E.A.; Lapina, S.S.; Klyachko-Gurvich, G.L.; Los, D.A. Lipid fatty acid composition and thermophilicity of cyanobacteria. *Russ. J. Plant Physiol.* **2004**, *51*, 353–360. [CrossRef]
53. Miyairi, S. CO_2 assimilation in a thermophilic cyanobacterium. *Energy Convers. Manag.* **1995**, *6–9*, 763–766. [CrossRef]
54. Petroutsos, D.; Amiar, S.; Abida, H.; Dolch, L.J.; Bastien, O.; Rebeille, F.; Jouhet, J.; Falconet, D.; Block, M.A.; McFadden, G.I.; et al. Evolution of galactoglycerolipid biosynthetic pathways—From cyanobacteria to primary plastids and from primary to secondary plastids. *Prog. Lipid Res.* **2014**, *54*, 68–85. [CrossRef] [PubMed]
55. Roels, J.A. *Energetics and Kinetics in Biotechnology*; Elsevier Biomedical Press: Amsterdam, The Netherlands, 1983.
56. Oliver, J.W.K.; Atsumi, S. Metabolic design for cyanobacterial chemical synthesis. *Photosynth. Res.* **2014**, *120*, 249–261. [CrossRef] [PubMed]
57. Shikanai, T.; Munekage, Y.; Kimura, K. Regulation of proton-to-electron stoichiometry in photosynthetic electron transport: Physiological function in photoprotection. *J. Plant Res.* **2002**, *115*, 3–10. [CrossRef] [PubMed]
58. Flamholz, A.; Noor, E.; Bar-Even, A.; Milo, R. eQuilibrator-the biochemical thermodynamics calculator. *Nucleic Acids Res.* **2012**, *40*, D770–D775. [CrossRef] [PubMed]
59. Noor, E.; Bar-Even, A.; Flamholz, A.; Lubling, Y.; Davidi, D.; Milo, R. An integrated open framework for thermodynamics of reactions that combines accuracy and coverage. *Bioinformatics* **2012**, *28*, 2037–2044. [CrossRef] [PubMed]
60. Raven, J.A.; Evans, M.C.W.; Korb, R.E. The role of trace metals in photosynthetic electron transport in O_2-evolving organisms. *Photosynth. Res.* **1999**, *60*, 111–149. [CrossRef]
61. Terzer, M.; Stelling, J. Large-scale computation of elementary flux modes with bit pattern trees. *Bioinformatics* **2008**, *24*, 2229–2235. [CrossRef] [PubMed]
62. Klahn, S.; Hagemann, M. Compatible solute biosynthesis in cyanobacteria. *Environ. Microbiol.* **2011**, *13*, 551–562. [CrossRef] [PubMed]
63. Beliaev, A.S.; Romine, M.F.; Serres, M.; Bernstein, H.C.; Linggi, B.E.; Markillie, L.M.; Isern, N.G.; Chrisler, W.B.; Kucek, L.A.; Hill, E.A.; et al. Inference of interactions in cyanobacterial-heterotrophic co-cultures via transcriptome sequencing. *ISME J.* **2014**, *8*, 2243–2255. [CrossRef] [PubMed]

64. Kim, Y.M.; Nowack, S.; Olsen, M.T.; Becraft, E.D.; Wood, J.M.; Thiel, V.; Klapper, I.; Kuhl, M.; Fredrickson, J.K.; Bryant, D.A.; et al. Diel metabolomics analysis of a hot spring chlorophototrophic microbial mat leads to new hypotheses of community member metabolisms. *Front. Microbiol.* **2015**, *6*. [CrossRef] [PubMed]
65. Senger, R.S. Biofuel production improvement with genome-scale models: The role of cell composition. *Biotechnol. J.* **2010**, *5*, 671–685. [CrossRef] [PubMed]
66. Hill, J.F.; Govindjee. The controversy over the minimum quantum requirement for oxygen evolution. *Photosynth. Res.* **2014**, *122*, 97–112. [CrossRef] [PubMed]
67. Kawamura, M.; Mimuro, M.; Fujita, Y. Quantitative relationship between two reaction centers in the photosynthetic system of blue-green algae. *Plant Cell Physiol.* **1979**, *20*, 697–705.
68. Sonoike, K.; Hihara, Y.; Ikeuchi, M. Physiological significance of the regulation of photosystem stoichiometry upon high light acclimation of *Synechocystis* sp. PCC 6803. *Plant Cell Physiol.* **2001**, *42*, 379–384. [CrossRef] [PubMed]
69. Vasilikiotis, C.; Melis, A. Photosystem-II reaction-center damage and repair cycle—Chloroplast acclimation strategy to irradiance stress. *Proc. Natl. Acad. Sci. USA* **1994**, *91*, 7222–7226. [CrossRef] [PubMed]
70. Folsom, J.P.; Parker, A.E.; Carlson, R.P. Physiological and proteomic analysis of *Escherichia coli* iron-limited chemostat growth. *J. Bacteriol.* **2014**, *196*, 2748–2761. [CrossRef] [PubMed]
71. Muramatsu, M.; Hihara, Y. Acclimation to high-light conditions in cyanobacteria: From gene expression to physiological responses. *J. Plant Res.* **2012**, *125*, 11–39. [CrossRef] [PubMed]
72. Rochaix, J.D. Regulation of photosynthetic electron transport. *Biochim. Biophys. Acta* **2011**, *1807*, 375–383. [CrossRef] [PubMed]
73. Kirilovsky, D. Photoprotection in cyanobacteria: The orange carotenoid protein (OCP)-related non-photochemical-quenching mechanism. *Photosynth. Res.* **2007**, *93*, 7–16. [CrossRef] [PubMed]
74. Li, G.; Brown, C.M.; Jeans, J.A.; Donaher, N.A.; McCarthy, A.; Campbell, D.A. The nitrogen costs of photosynthesis in a diatom under current and future pCO_2. *New Phytol.* **2015**, *205*, 533–543. [CrossRef] [PubMed]
75. Murphy, C.D.; Roodvoets, M.S.; Austen, E.J.; Dolan, A.; Barnett, A.; Campbell, D.A. Photoinactivation of photosystem II in *Prochlorococcus* and *Synechococcus*. *PLoS ONE* **2017**, *12*, e0168991. [CrossRef] [PubMed]
76. Edwards, J.S.; Ibarra, R.U.; Palsson, B.O. In silico predictions of *Escherichia coli* metabolic capabilities are consistent with experimental data. *Nat. Biotechnol.* **2001**, *19*, 125–130. [CrossRef] [PubMed]
77. Goldberg, I.; Rock, J.S.; Ben-Bassat, A.; Mateles, R.I. Bacterial yields on methanol, methylamine, formaldehyde, and formate. *Biotechnol. Bioeng.* **1976**, *18*, 1657–1668. [CrossRef] [PubMed]
78. Hunt, K.A.; Jennings, R.D.; Inskeep, W.P.; Carlson, R.P. Stoichiometric modeling of assimilatory and dissimilatory biomass utilization in a microbial community. *Environ. Microbiol.* **2016**, *18*, 4946–4960. [CrossRef] [PubMed]
79. Janssen, P.H.; Hugenholtz, P. Fermentation of glycolate by a pure culture of a strictly anaerobic gram-positive bacterium belonging to the family *Lachnospiraceae*. *Arch. Microbiol.* **2003**, *179*, 321–328. [CrossRef] [PubMed]
80. Luttik, M.A.H.; Van Spanning, R.; Schipper, D.; Van Dijken, J.P.; Pronk, J.T. The low biomass yields of the acetic acid bacterium *Acetobacter pasteurianus* are due to a low stoichiometry of respiration-coupled proton translocation. *Appl. Environ. Microbiol.* **1997**, *63*, 3345–3351. [PubMed]
81. Nagpal, S.; Chuichulcherm, S.; Livingston, A.; Peeva, L. Ethanol utilization by sulfate-reducing bacteria: An experimental and modeling study. *Biotechnol. Bioeng.* **2000**, *70*, 533–543. [CrossRef]
82. Seifritz, C.; Frostl, J.M.; Drake, H.L.; Daniel, S.L. Glycolate as a metabolic substrate for the acetogen *Moorella thermoacetica*. *FEMS Microbiol. Lett.* **1999**, *170*, 399–405. [CrossRef]
83. Bernstein, H.C.; McClure, R.S.; Hill, E.A.; Markillie, L.M.; Chrisler, W.B.; Romine, M.F.; McDermott, J.E.; Posewitz, M.C.; Bryant, D.A.; Konopka, A.E.; et al. Unlocking the constraints of cyanobacterial productivity: Acclimations enabling ultrafast growth. *mBio* **2016**, *7*. [CrossRef] [PubMed]
84. Cole, J.K.; Hutchison, J.R.; Renslow, R.S.; Kim, Y.M.; Chrisler, W.B.; Engelmann, H.E.; Dohnalkova, A.C.; Hu, D.H.; Metz, T.O.; Fredrickson, J.K.; et al. Phototrophic biofilm assembly in microbial-mat-derived unicyanobacterial consortia: Model systems for the study of autotroph-heterotroph interactions. *Front. Microbiol.* **2014**, *5*. [CrossRef] [PubMed]
85. Paerl, H.W.; Pinckney, J.L. A mini-review of microbial consortia: Their roles in aquatic production and biogeochemical cycling. *Microb. Ecol.* **1996**, *31*, 225–247. [CrossRef] [PubMed]

86. Paerl, H.W.; Pinckney, J.L.; Steppe, T.F. Cyanobacterial-bacterial mat consortia: Examining the functional unit of microbial survival and growth in extreme environments. *Environ. Microbiol.* **2000**, *2*, 11–26. [CrossRef] [PubMed]
87. Gubernator, B.; Bartoszewski, R.; Kroliczewski, J.; Wildner, G.; Szczepaniak, A. Ribulose-1,5-bisphosphate carboxylase/oxygenase from thermophilic cyanobacterium *Thermosynechococcus elongatus*. *Photosynth. Res.* **2008**, *95*, 101–109. [CrossRef] [PubMed]
88. Falkowski, P.G.; Raven, J.A. *Aquatic Photosynthesis*, 2nd ed.; Princeton University Press: Princeton, NJ, USA, 2007.
89. Savir, Y.; Noor, E.; Milo, R.; Tlusty, T. Cross-species analysis traces adaptation of rubisco toward optimality in a low-dimensional landscape. *Proc. Natl. Acad. Sci. USA* **2010**, *107*, 3475–3480. [CrossRef] [PubMed]
90. Tcherkez, G.G.B.; Farquhar, G.D.; Andrews, T.J. Despite slow catalysis and confused substrate specificity, all ribulose bisphosphate carboxylases may be nearly perfectly optimized. *Proc. Natl. Acad. Sci. USA* **2006**, *103*, 7246–7251. [CrossRef] [PubMed]
91. Mangan, N.M.; Flamholz, A.; Hood, R.D.; Milo, R.; Savage, D.F. pH determines the energetic efficiency of the cyanobacterial CO_2 concentrating mechanism. *Proc. Natl. Acad. Sci. USA* **2016**, *113*, E5354–E5362. [CrossRef] [PubMed]
92. Bateson, M.M.; Ward, D.M. Photoexcretion and fate of glycolate in a hot-spring cyanobacterial mat. *Appl. Environ. Microbiol.* **1988**, *54*, 1738–1743. [PubMed]
93. Huege, J.; Goetze, J.; Schwarz, D.; Bauwe, H.; Hagemann, M.; Kopka, J. Modulation of the major paths of carbon in photorespiratory mutants of *Synechocystis*. *PLoS ONE* **2011**, *6*, e16278. [CrossRef] [PubMed]
94. Yokota, A.; Iwaki, T.; Miura, K.; Wadano, A.; Kitaoka, S. Model for the relationships between CO_2-concentrating mechanism, CO_2 fixation, and glycolate synthesis during photosynthesis in *Chlamydomonas-reinhardtii*. *Plant Cell Physiol.* **1987**, *28*, 1363–1376.
95. Jordan, D.B.; Ogren, W.L. The CO_2/O_2 specificity of ribulose 1,5-bisphosphate carboxylase oxygenase—Dependence on ribulosebisphosphate concentration, pH and temperature. *Planta* **1984**, *161*, 308–313. [CrossRef] [PubMed]
96. Sander, R. Compilation of Henry's law constants (version 4.0) for water as solvent. *Atmos. Chem. Phys.* **2015**, *15*, 4399–4981. [CrossRef]
97. Gerstl, M.P.; Jungreuthmayer, C.; Zanghellini, J. tEFMA: Computing thermodynamically feasible elementary flux modes in metabolic networks. *Bioinformatics* **2015**, *31*, 2232–2234. [CrossRef] [PubMed]
98. Peres, S.; Jolicoeur, M.; Moulin, C.; Dague, P.; Schuster, S. How important is thermodynamics for identifying elementary flux modes? *PLoS ONE* **2017**, *12*, e0171440. [CrossRef] [PubMed]
99. Herbert, D.; Phipps, P.J.; Strange, R.E. Chemical analysis of microbial cells. In *Methods in Microbiology*; Norris, J.R., Ribbons, D.W., Eds.; Academic Press: New York, NY, USA, 1971; pp. 209–344.
100. Carnicer, M.; Baumann, K.; Toplitz, I.; Sanchez-Ferrando, F.; Mattanovich, D.; Ferrer, P.; Albiol, J. Macromolecular and elemental composition analysis and extracellular metabolite balances of *Pichia pastoris* growing at different oxygen levels. *Microb. Cell Fact.* **2009**, *8*. [CrossRef] [PubMed]
101. Elser, J.J.; Bracken, M.E.S.; Cleland, E.E.; Gruner, D.S.; Harpole, W.S.; Hillebrand, H.; Ngai, J.T.; Seabloom, E.W.; Shurin, J.B.; Smith, J.E. Global analysis of nitrogen and phosphorus limitation of primary producers in freshwater, marine and terrestrial ecosystems. *Ecol. Lett.* **2007**, *10*, 1135–1142. [CrossRef] [PubMed]
102. Johnson, D.B.; Kanao, T.; Hedrich, S. Redox transformations of iron at extremely low pH: Fundamental and applied aspects. *Front. Microbiol.* **2012**, *3*, 96. [CrossRef] [PubMed]
103. Kliphuis, A.M.J.; Klok, A.J.; Martens, D.E.; Lamers, P.P.; Janssen, M.; Wijffels, R.H. Metabolic modeling of *Chlamydomonas reinhardtii*: Energy requirements for photoautotrophic growth and maintenance. *J. Appl. Phycol.* **2012**, *24*, 253–266. [CrossRef] [PubMed]